

Title	Geometrical and causal relation between the rupture geometry of a mainshock and distribution of the faults of the aftershocks : the 1995 Hyogo-ken Nanbu earthquake sequence, Japan( Dissertation_全文 )
Author(s)	Cho, Ikuo
Citation	Kyoto University (京都大学)
Issue Date	1999-03-23
URL	<a href="http://dx.doi.org/10.11501/3149351">http://dx.doi.org/10.11501/3149351</a>
Right	
Type	Thesis or Dissertation
Textversion	author

GEOMETRICAL AND CAUSAL RELATION BETWEEN THE  
RUPTURE GEOMETRY OF A MAINSHOCK AND THE  
DISTRIBUTION OF THE FAULTS OF THE AFTERSHOCKS: THE  
1995 HYOGO-KEN NANBU EARTHQUAKE SEQUENCE, JAPAN

BY IKUO CHO

ABSTRACT

Applying a method based on the fuzzy theory to the aftershock distribution within 5 days after the 1995 Hyogo-ken Nanbu earthquake, Japan, we have estimated the distribution of the faults on which the aftershocks occur. The fault distribution suggests that the aftershocks occurred on numerous small faults rather than on a simple planar fault surface. The fault distribution is compared with the rupture geometry of the mainshock that is estimated without referring to the aftershock distribution. Not depending on the data period, the faults of the aftershocks are not distributed in the regions of large slip of the mainshock, and the faults of at least the large aftershocks are distributed near the bends or edges of the mainshock rupture. We calculate  $\Delta CFF$  and find that the distribution of the faults on which the large aftershocks occur is consistent with the mainshock-induced stress changes. There are several clusters of faults of aftershocks in the shallow regions at depths from 4 to 9 km on the northeast side, which consist of the faults of the small aftershocks. They are triggered by the changes in pore pressure or hydraulic fracturing induced by an interaction between the rupture geometry of the mainshock and pore fluid.

INTRODUCTION

The slip distribution of a mainshock can be obtained on a fine scale due to recent development in the inversion method of a dislocation model (Hartzell and Heaton, 1985; Olson and Apsel, 1983), and then the slip distribution can be compared with the aftershock distribution in detail (e.g., Mendoza and Hartzell, 1988). However, the rupture geometry<sup>1</sup> of a mainshock has

---

<sup>1</sup>Throughout this study the term "rupture geometry" of a mainshock is used as the term "fault geometry" of a mainshock in order to avoid confusing with the term "fault distribution" of the aftershocks.

been difficult to be compared with the aftershock distribution because it is estimated from the aftershock distribution in most cases. Cho and Nakanishi (1998) (hereafter CN98) estimates the three-dimensional rupture geometry of the 1995 Hyogo-ken Nanbu earthquake using a linear inversion of the strong-motion and geodetic data without referring to the aftershock distribution. We can examine in detail the relation between the rupture geometry of the mainshock and the aftershock distribution.

Aftershocks typically occur over the entire rupture area and its surroundings, although they are expected to cluster in regions where large stress concentrations are produced (e.g., Aki, 1979; Das and Scholtz, 1981; Rybicki, 1973; Scholtz, 1990). Then an aftershock data set is usually sorted by magnitude and is divided into time sections so that we can find meaningful clusters of aftershocks. This way is usual but is sometimes inappropriate to find clusters of aftershocks in time. There is no general rule to determine a time interval at which an aftershock data set is divided into time sections. For the purpose of finding such clusters of aftershocks, we can not utilize the clustering or window methods that have been developed for identification of aftershocks (e.g., Davis and Frohlich, 1991; Frohlich and Davis, 1985; Molchan and Dmitrieva, 1992; Gardner and Knopoff, 1974; Prozorov and Dziewonski, 1982; Reasenber, 1985). Most of these methods need physical basis to describe aftershock behaviors for determining spatial and temporal thresholds by which aftershocks are identified. Nevertheless, the relation between an aftershock and the aftershock sequences of their own has never been examined in detail. Such thresholds that are physically determined are not used in Single-link cluster analysis (Frohlich and Davis, 1985; Davis and Frohlich, 1991), but instead, a great deal of efforts is required to optimize parameters that play a role of such thresholds.

The fuzzy theory has been developed since Zadeh (1965) suggested a fuzzy set in order to deal with sets which do not have sharply defined boundaries. That is, the fuzzy theory stands on a concept that is opposite from classification according to sharply defined thresholds. The fuzzy theory has been advanced with intent to model human information processing principles seen in control, pattern recognition, reasoning, decision making, and database queries. It will be easy to understand that an approach based on the fuzzy theory is effective when our intuitive perception seems rather valid but physical, mathematical, or statistical models that support the perception

can not be made in nature or have not been established. Such situations frequently arise in the fields of earth sciences with respect to earthquakes. Yokota and Ito (1994) (hereafter YI94) discusses applicability of the fuzzy theory to seismology, for example, attempts at earthquake prediction using fuzzy clustering (e.g., Feng et al., 1985; Feng and Ichikawa, 1989) or fuzzy fractal; fuzzy description of geological data (Yokota and Masumoto, 1984); fuzzy database queries with respect to historical and destructive earthquakes, seismicity, and earthquake precursor; and fuzzy analysis of information on seismic intensity obtained through questionnaires.

Hoshihara et al. (1993) applies the fuzzy theory to a kind of clustering method in which any thresholds are not required. Based on a concept similar to that of Hoshihara et al. (1993), YI94 devises a method estimating distribution of the faults on which earthquakes occur. In this study the distribution of the faults on which the aftershocks occur is estimated from the aftershock distribution of the 1995 Hyogo-ken Nanbu earthquake, using the method of YI94 with modifications. The distribution of the faults of the aftershocks estimated is compared with the rupture geometry of the mainshock, the slip distribution of the mainshock that is obtained using the three-dimensional rupture geometry, and the distribution of the mainshock-induced stress changes.

## DISLOCATION MODEL OF THE MAINSHOCK

### *Data and Method*

As shown in Figure 1, the 1995 Hyogo-ken Nanbu earthquake occurred in inland area, which is dense with both the strong-motion stations and the observation points of geodetic data. The strong-motion data consist of 17 vertical and 32 horizontal components of the waveforms recorded at 18 stations. The stations are deployed by the Japan Meteorological Agency (JMA), the Committee of Earthquake Observation and Research in the Kansai Area (CEORKA), and the Disaster Prevention Research Institute, Kyoto University (DPRI). The geodetic data consist of 105 vertical static displacements of leveling benchmarks, 51 static line-length changes between triangulation points, and 34 components of horizontal static displacements at the Global Posi-

tioning System (GPS) stations, which are taken from Hashimoto et al. (1996). This data set and the calculation of Green's functions are the same as used in CN98.

The dislocation model of the mainshock of the 1995 Hyogo-ken Nanbu earthquake is obtained using a multi-window method (Hartzell and Heaton, 1985; Olson and Apsel, 1983). As shown in Figure 2, rectangular subfaults are arranged in three dimensions based on the rupture geometry estimated by CN98. The orientation of each subfault is determined so that the entire fault surface can be smooth. The size of each subfault is 4 km long in the direction of the strike and 5 km long in the direction of the dip. Following CN98, the slipped regions beneath Akashi strait and Awaji Island (the southwest part in the studied region) would almost reach the surface. Then, the upper edges of the subfaults in the shallowest regions beneath Akashi strait and Awaji Island are moved toward the surface. The size of these modified subfaults is 4 km long in the direction of the strike and about 6.5 km long in the direction of the dip (Fig. 2). We use three time windows at intervals of 1 s, each of which is a moment-rate function of triangular (0.5 s, 0.5 s). The source time function at each subfault is represented by a weighted sum of the three time windows. Thus, the duration of a source time function at each subfault is 3 s. The rupture front propagates at a constant rupture velocity from the hypocenter ( $34.600^\circ\text{N}$ ,  $135.0399^\circ\text{E}$ , 14.0 km, 20:46:51.9, January 16 (GMT)) that is located by CN98.

In the inversion, the geodetic data are scaled so that the square sum of the geodetic data can equal that of the strong-motion data. Then, the geodetic data are multiplied by a weight  $W_g$  so that we can examine the influence of the geodetic data on the inversion by changing  $W_g$ . To stabilize the inversion, we append a smoothing constraint (Hartzell and Heaton, 1983) and a nonnegative constraint to confine the slip angles within  $180 \pm 45^\circ$ . The nonnegative least-squares problem is solved using routine NNLS from Lawson and Hanson (1974).

### *Results*

The misfits between the observed and synthetic records vary slightly according to the rupture velocity where  $W_g$  is fixed with 1.0 (Fig. 3). The slight variation in respective misfits of the strong-motion and geodetic data are due to the facts that the time windows allow for uncertainty with respect to rupture velocity, and that static displacements do not depend on rupture velocity.

As indicated by the slight variation in misfits, the influence of rupture velocity on the dislocation model is slight. There is no criterion for determining the rupture velocity except adopting the rupture velocity that minimizes the misfit. We can see that the rupture velocity of 3.4 km/s provides the smallest misfit of the strong-motion data.

Figure 4 shows the misfits between the observed and synthetic records as functions of  $W_g$  at a rupture velocity of 3.4 km/s. The misfits of the strong-motion and geodetic data are evenly balanced when  $W_g = 1.0$ . The misfit of the geodetic data seldom changes with  $W_g$  larger than 1.0, while the misfit of the strong-motion data increases remarkably. The opposite is observed with  $W_g$  less than 1.0. This fact suggests that the scaling of the geodetic data in which the square sum of the geodetic data can equal that of the strong-motion data is appropriate.

The influence of the geodetic data on the inversion can be examined by comparing the dislocation models obtained from separate inversions with different values of  $W_g$ . Figure 5 compares the dislocation models with  $W_g$  of 0.0, 1.0, 5.0, and infinity at a rupture velocity of 3.4 km/s. We find that in the shallow region beneath Awaji Island, the slip amplitudes obtained from only the strong-motion data ( $W_g = 0.0$ ) are 0.9 m at most, while they range from 2.1 to 2.6 m when the geodetic data are used. The dislocation model obtained from the geodetic data would be reliable in the shallow region beneath Awaji Island, because Awaji Island is very dense with the geodetic stations rather than the strong-motion stations. Therefore the slip amplitude in the shallow region beneath Awaji Island would reach at least about 2.0 m. However in general, if slip in a shallow region is large, an accurate inversion of slip in the deep region is difficult from the geodetic data. Regarding with the deep regions beneath Awaji Island, we should refer to the dislocation models obtained with small  $W_g$  in which the strong-motion data are relatively weighted. The dislocation models obtained with  $W_g$  of 0.0 and 1.0 indicate that the deep region beneath the Awaji Island does not slip much. The large slip in the deep region beneath Awaji Island seen in the dislocation model obtained with large  $W_g$  will be artificial. The smoothing constraint would influence the inversion more than the strong-motion data when the geodetic data is much weighted, and then the large slip in the shallow region results in the large slip in the deep region. It is reliable that the shallow region beneath Awaji Island, the deep region beneath Akashi strait, and the deep region on the Kobe side (the northeast side in the studied

region) slip more than the surrounding regions, because this tendency is commonly found with all values of  $W_g$ .

The slip pattern of the dislocation model with  $W_g$  of 1.0 at rupture velocity of 3.4 km/s fulfills the requirements that are set in this examination. We consider that the dislocation model with  $W_g$  of 1.0 at rupture velocity of 3.4 km/s is optimal, and simply refer to it as the dislocation model hereafter. The moment release that is calculated from the dislocation model totals  $1.2 \times 10^{19}$  ( $M_w$ 6.7). The respective misfits of the strong-motion data and the geodetic data are 49 % and 15 %. The dislocation model shows that the slip in the shallow region beneath Akashi strait is very small, suggesting that the rupture zone in the shallow regions on the Awaji side does not reach the Kobe side over Akashi strait. The slip in the shallow region on the Kobe side is also very small, although at the surface above the corresponding region there is a narrow band called the severely damaged zone of about 1.5 km wide and 22 km long with the seismic intensity of seven on a JMA (Japan Meteorological Agency) scale (JMA, 1995). The synthetic waveforms (Fig. 6) and static displacements (Fig. 7) calculated for the dislocation model match the data fairly well.

In order to examine the influence of the source time function on the inversion, we use seven time windows at intervals of 0.5 s, each of which is a moment-rate function of triangular (0.5 s, 0.5 s). Thus, the duration of a source time function at each subfault is 4 s. Changing only the source time function, we make the same inversion with  $W_g$  of 1.0 at a rupture velocity of 3.4 km/s. The resulting dislocation model has great resemblance to that obtained from the inversion with three time windows. The moment release that is calculated from this dislocation model totals  $1.3 \times 10^{19}$  ( $M_w$ 6.7). The respective misfits of the strong-motion data and the geodetic data are 46 % and 13 %. The number of model parameters is 2.3 times as large as that used in the inversion with three time windows, but the respective misfits decrease only 3 % and 2 %. We conclude that three time windows are sufficient for the dislocation model of the 1995 Hyogo-ken Nanbu earthquake.

ESTIMATION OF THE DISTRIBUTION OF THE FAULTS ON WHICH THE AFTERSHOCKS OCCUR

### *Method Based on the Fuzzy Sets*

We use the method of YI94 with modifications to estimate the distribution of the faults on which the aftershocks of the 1995 Hyogo-ken Nanbu earthquake occur. The method of YI94 stands on a hypothesis that if earthquakes are close in space and time, the fault surfaces on which the earthquakes occur is common. According to the hypothesis, in a region with seismic activity, we can illustrate the distribution of the faults on which earthquakes occur by a frame composed of segments each of which connects two hypocenters of earthquakes close in space and time. This hypothesis would be at least approximately correct but has a problem that the term “close” is linguistic rather than numerical. The problem is due to the fact that we have no physical basis to determine a threshold by which we can identify earthquakes close in space and time that occur on a common fault surface. In order to deal with this problem YI94 introduces the concept of fuzzy sets.

Fuzzy sets are devised by Zadeh (1965), in order to deal with sets which do not have sharply defined boundaries, for instance, a set of all real numbers which are much greater than 1, a set of old men, or a set of beautiful women. Zadeh (1965) defines a fuzzy set  $A$  in  $X$ , where  $X$  is a space of points with a generic element of  $X$  denoted by  $x$ , as a set characterized by a membership function  $f_A(x)$  which associates with each point in  $X$  a real number in the interval  $[0, 1]$ , with the value of  $f_A(x)$  at  $x$  representing the “grade of membership” of  $x$  in  $A$ . The grade of the membership describes the degree of compatibility of  $x$  with the concept represented by the fuzzy set. Grade 0 denotes total incompatibility, and grade 1 total compatibility. Zadeh (1965) illustrates a membership function by the following example. Let  $X$  be the real line  $R^1$  and let  $A$  be a fuzzy set of numbers which are much greater than 1. Then one can give a precise, though subjective, characterization of  $A$  by specifying  $f_A(x)$  as a function on  $R^1$ . Representative values of such a function might be:  $f_A(0) = 0$ ;  $f_A(1) = 0$ ;  $f_A(5) = 0.01$ ;  $f_A(10) = 0.2$ ;  $f_A(100) = 0.95$ ;  $f_A(500) = 1$ . It should be noted that although a membership function has some resemblance to a probability function or a probability density function, the concept of a fuzzy set completely nonstatistical in nature (Zadeh, 1965). The grade has no physical meaning.

There is no general rule to define a membership function because a fuzzy set deals with

linguistic, imprecise concepts. In the case of a set of old men, the range of age compatible with the term “old” will vary according to not only person but also country, culture, or the times. It is unavoidable that a membership function tends to be defined rather subjectively. However, because the most important role of the membership function is determination of greater or less on ordinal scale that is mentioned in Stevens (1946), the detailed form of a membership function may not be a problem. Therefore as suggested by Zadeh (1975), it may be convenient to standardize membership functions with adjustable parameters.

In the method of YI94, fuzzy sets X and Y that are composed of pairs of earthquakes close in space and time, characterized by membership functions  $R^d(\Delta r_{ij})$  and  $R^t(\Delta t_{ij})$  respectively are introduced, where  $\Delta r_{ij}$  is the distance between two earthquakes  $i$  and  $j$ , and  $\Delta t_{ij}$  is the absolute value of the difference in origin time. The grade describes the degree of compatibility of  $\Delta r_{ij}$  or  $\Delta t_{ij}$  with the concept of closeness. In terms of the fuzzy sets X and Y, an assertion of the form “two earthquakes are close” is interpreted as the assignment of a linguistic rather than a numerical value to the closeness of the two earthquakes, that is, the membership functions  $R^d$  and  $R^t$  are not defined on physical basis. According to YI94 we assume that respective closeness in space and time decreases exponentially with the increase of  $\Delta r_{ij}$  and  $\Delta t_{ij}$ . We define the membership functions with adjustable parameters  $A^d$  and  $A^t$  that control the ranges of transition from total compatibility to total incompatibility of  $\Delta r_{ij}$  and  $\Delta t_{ij}$  with the concept of closeness respectively as follows (Figure 8a and Figure 8b).

$$R^d(\Delta r_{ij}) = \frac{2}{1 + \exp(\Delta r_{ij}/A^d)} \quad (1)$$

and

$$R^t(\Delta t_{ij}) = \frac{2}{1 + \exp(\Delta t_{ij}/A^t)}. \quad (2)$$

In order to define closeness in both space and time, YI94 takes the intersection of the two fuzzy sets X and Y in the fuzzy-set-theoretic sense, which is the largest fuzzy set contained in both X and Y whose membership function  $R$  is related to  $R^d$  and  $R^t$  by

$$R(\Delta r_{ij}, \Delta t_{ij}) = R^d(\Delta r_{ij}) \wedge R^t(\Delta t_{ij}), \quad (3)$$

where  $\wedge$  stands for minimum (Figure 8c). We can see from Figure 8c that the values of  $R$  are the same at A and B. That is, values of  $R$  are not changed in a range of  $\Delta r_{ij}$  smaller than a

threshold, where  $\Delta t_{ij}$  is fixed. Similarly, values of  $R$  are not changed in a range of  $\Delta t_{ij}$  smaller than a threshold, where  $\Delta r_{ij}$  is fixed. This fact means that we are required to determine such thresholds, and then the forms of  $R^d$  and  $R^t$  should be examined critically. A physical basis to define  $R^d$  and  $R^t$  may be required.

Because we do not have a physical basis on which the thresholds are determined, it would be more preferable to consider that the degree of closeness in both space and time continues to increase with decrease of  $\Delta r_{ij}$  where  $\Delta t_{ij}$  is fixed. According to Hoshiya et al. (1983), we take the algebraic product of the two fuzzy sets X and Y, which is defined in terms of the membership functions of X and Y by the relation below (Figure 8d).

$$R(\Delta r_{ij}, \Delta t_{ij}) = R^d(\Delta r_{ij})R^t(\Delta t_{ij}). \quad (4)$$

We can see from Figure 8d that the values of  $R$  defined by equation (4) are not the same at A and B. We can distinguish among values of  $R$  in whole range of  $\Delta r_{ij}$  with  $\Delta t_{ij}$  fixed. The membership function  $R$  that is defined in equation (4) plays an important role in determining greater or less in whole range of  $\Delta r_{ij}$  with  $\Delta t_{ij}$  fixed. Therefore we do not have to determine the thresholds as mentioned above. The problem about the detailed forms of  $R^d$  and  $R^t$  is resolved by using equation (3).

In reality, a fault that is represented by segment connecting two hypocenters has a finite area, and there are hypocentral errors. It is incomplete to consider segment connecting two hypocenters close in both space and time as a fault due to these realities. According to YI94, we introduce a membership function  $f(\rho_{ij}(P))$  that is a monotonically decreasing function, where  $\rho_{ij}(P)$  is the shortest distance from point P to segment  $\bar{i}\bar{j}$ .  $f$  is defined as  $f(\rho_{ij}) = 1/(\rho_{ij} + 1)^2$  in this study. Then according to YI94, we define the grade of a membership function  $Rf$  as the compatibility with the concept that point P belongs to the fault represented by segment  $\bar{i}\bar{j}$ . That is, in order to deal with the realities we accept the possibility that point P belongs to the fault represented by segment  $\bar{i}\bar{j}$  not only on the segment but also in the vicinity.

Note that the concept of fuzzy set can be applied to the concept of possibility. According to the theory of possibility based on fuzzy sets (Zadeh, 1978), a fuzzy set characterized by the membership function  $Rf$  can be considered as a possibility distribution that is associated

with point P by the proposition “point P belongs to the fault represented by segment  $\bar{i}\bar{j}$ .” A possibility distribution plays a role analogous with a probability distribution in the probability theory. The detailed description of the theory of possibility is found in Zadeh (1978). According to the theory of possibility, the possibility measure (Zadeh, 1978),  $\mu(P)$ , that point P belongs to a fault where all combination of  $i$  and  $j$  are considered can be expressed as

$$\mu(P) = \bigvee_{i,j} R(\Delta r_{ij}, \Delta t_{ij}) f(\rho_{ij}(P)), \quad (5)$$

where  $\bigvee_{i,j}$  stands for maximum over all combination of  $i$  and  $j$ . The higher  $\mu(P)$  becomes the higher the possibility that point P belongs to a fault becomes. Note that the possibility  $\mu(P)$  measure has no physical meaning and possibility has no relation with probability. We may represent the fuzzy set Z composed of points that belong to the faults on which aftershocks occur in the form

$$Z = \int_{\mathbf{w}} \mu(P)/P \quad (6)$$

where the integral sign stands for the union of the constituent fuzzy singletons  $\mu(P)/P$ . Following the definition of Zadeh (1973), if  $A$  is a fuzzy singleton whose support is a single point  $y$ , we write  $A = \mu/y$  where  $\mu$  is the grade of membership of  $y$  in  $A$ , and the symbol  $/$  is a separator employed for disambiguation. Hereafter Z is referred to the distribution of the faults on which aftershocks occur.

As shown in Figure 8a and Figure 8b, the ranges of transition from total compatibility to total incompatibility of  $\Delta r_{ij}$  and  $\Delta t_{ij}$  with the concept of closeness vary with  $A^d$  and  $A^t$ , respectively. The changes in grade are large within specified ranges of  $\Delta r_{ij}$  and  $\Delta t_{ij}$ , while they are very slight out of the ranges. Then, we can seldom identify the changes in grade out of the ranges if the distribution of the faults on which the aftershocks occur that we estimate is illustrated by contours at uniform intervals, although it is possible in nature. We adjust  $A^d$  and  $A^t$  only for convenience of illustration of resulting distributions. In order to determine the values of  $A^d$  and  $A^t$ , we estimate the distribution of the faults of the aftershocks, changing the values of  $A^d$  and  $A^t$ , and compare the resulting distributions with the aftershock distribution. According to the comparison, we use the values of  $A^d$  0.91 and  $A^t$  0.45.

### *Results*

More than 2,000 hypocenters of aftershocks within 5 days after the mainshock, which occurred near mainshock rupture zone (within a rectangle in Figure 2a), are used in the analysis. The earlier portion of the aftershock data before 7:00, January 17, 1995 (GMT) is taken from Nemoto et al. (1996). The hypocentral errors for 90 % of the aftershocks do not exceed 0.5 and 1.0 km in the horizontal and vertical directions, respectively. The later portion is taken from Katao (*personal communication*), who relocates the hypocenters that are determined automatically using data from the Abuyama Seismological Observatory operated by Disaster Prevention Research Institute, Kyoto University. The hypocentral errors average at 0.6 and 0.7 km in the horizontal and vertical directions respectively on the Kobe side, while the hypocentral errors average at 1.2 and 2.0 km in the horizontal and vertical directions respectively on the Awaji side.

Figure 9 compares between the slip distribution of the mainshock obtained and the distribution of the faults on which the aftershocks occur. The corresponding aftershock distribution is also shown in the figure. We can see that the possibility measure is low in the regions of large slip, which are located in the shallow region beneath Awaji Island, in the deep region beneath Akashi strait, and in the deep region on the Kobe side. Aftershocks are seldom seen in these regions. The possibility measure is high in the regions at middle depths on the Awaji and Kobe sides. In the regions of high possibility measure we can see local peaks: the number of peaks of high possibility measure is not single.

Figure 10a shows the horizontal sections comparing between the rupture geometry of the mainshock and the distribution of the faults on which the aftershocks occur. We can see clearly that the local peaks of high possibility measure, at which the rupture due to aftershocks would progress markedly, are located near the bends or edges of the mainshock rupture. At a depth of 4 km on the Kobe side, near neither a bend nor an edge of the mainshock rupture, there is a region of high possibility measure.

From the comparison of Figure 10a and Figure 10b, we can see that the regions of high possibility measure tend to cluster in the regions of many aftershocks. However, it should be noticed that the number of aftershocks does not have direct relation to the estimation of the fault distribution, because a possibility measure at each point is determined by a single pair

of aftershocks in the vicinity having a highest grade of membership function  $R$  represented by equation (4). Therefore it might be possible that the estimate of the fault distribution is strongly biased by a single pair in the vicinity whose grade  $R$  represented by equation (4) is abnormally high compared to the average of the vicinity. In order to examine this bias, we estimate the distribution of the faults on which the aftershocks occur, taking the second maximum instead of the maximum in equation (5). Figure 11 shows that the main feature does not change, although the possibility measure decreases to nearly zero in some regions where the aftershocks are few at depths from 14 to 19 km on the Kobe side. The bias reveals to be very slight.

In order to compare the distribution of the faults on which the aftershocks occur with the large-scale rupture geometry of the mainshock, it might be preferable to use the data consisting of only large aftershocks because the generation of the small aftershocks would be easily influenced by inhomogeneities in rupture geometry on finer scale than the scale that we can deal with. Then, we estimate the fault distribution using data sets from which the small aftershocks are excluded, changing the lower limit of the magnitude ( $M_{low}$ ) from 1.0 to 3.0. In Figure 12, the possibility measure decreases on the Kobe side significantly when  $M_{low}$  is 3.0, and some regions of high possibility measure disappear, including the region of high possibility measure at a depth of 4 km on the Kobe side in Figure 10a. Not biased by the smaller aftershocks, the faults of aftershocks larger than the magnitude of 3.0 are located near the bends or edges of the large-scale mainshock rupture on both Awaji and Kobe sides. Figure 12 shows that the rupture progresses mainly due to the aftershocks smaller than the magnitude of 3.0 on the Kobe side, in particular, at depths from 4 to 9 km. On the other hand, the changes in possibility measure are very slight on the Awaji side. The rupture progresses mainly due to aftershocks larger than the magnitude of 3.0 on the Awaji side. This tendency does not come from the difference in detectability due to the density of the seismic stations between the Awaji and Kobe sides because the lower limit of the magnitude at which distribution of the possibility measure on the Kobe side is changed remarkably is as large as  $M_{low}$  of 3.0.

We can see from Figure 12 that on the Kobe side at a depth of 14 km, the local peaks of high possibility measure for small aftershocks with magnitude less than 2.0 are significantly broadened as compared with those for large aftershocks with magnitude larger than 3.0. That is, the faults

of the large aftershocks at a depth of 14 km on the Kobe side is surrounded by the faults of the small aftershocks. In the region near the bend at a depth of 9 km on the Awaji side, the faults of the large aftershocks with magnitude larger than 3.0 is surrounded by the faults of the small aftershocks with magnitude smaller than 1.0. The large aftershocks near the bends at a depth of 14 km on the Kobe side and at a depth of 9 km on the Awaji side seems to have smaller aftershock sequences of their own.

In order to examine temporal variation in fault distribution, we sort the aftershock data by the following periods: a period from the mainshock to 1 hour after; a period from the mainshock to 1 day after; a period from 1 to 2 days after the mainshock; a period from 2 to 5 days after the mainshock. The fault distribution is estimated using each data set. Figure 13 shows that the local peaks of high possibility measure tend to be located near the bends and edges of the mainshock rupture in every data period. That is, this tendency does not depend on the data period. We can see a remarkable difference in time dependency of appearance of the local peaks between the Awaji side and the Kobe side. On the Awaji side, the possibility measure becomes high in the first period, and significantly decreases in the third period. On the Kobe side, the possibility measure becomes high behind the Awaji side, and the high values continue to the fourth period.

On the Kobe side the region of high possibility measure is located at a depth of 14 km in the first period. In the second period, the regions at depths from 4 to 9 km become major regions of high possibility measure, although the possibility measure is still high at a depth of 14 km. The possibility measure at depths from 4 to 9 km keeps high values in the third and fourth periods. The possibility measure at a depth of 14 km decreases significantly in the third period and increases again in the fourth period, but the increase is very slight. Only small aftershocks contribute to the high possibility measure on the Kobe side as mentioned in Figure 12, and then we can say that the rupture continues to progress moving upward on the Kobe side, accompanied with small aftershocks.

We can see that the local peak of high possibility measure on the Kobe side in the first period splits into three local peaks at depths from 9 to 14 km in the second period. The local peak of high possibility measure on the Kobe side in the first period well corresponds to the local peak

with  $M_{\text{low}}$  of 3.0 found in Figure 12, while the three local peaks at depths from 9 to 14 km in the second period correspond to the local peaks with  $M_{\text{low}}$  of both 1.0 and 2.0 found in Figure 12. The large aftershocks seen in the first period at a depth of 14 km on the Kobe side result in smaller aftershock sequences of their own in the second period. In the region near the bend at a depth of 9 km on the Awaji side, the faults of the large aftershocks with magnitude larger than 3.0 seen in the first period are surrounded by the faults of the small aftershocks with magnitude smaller than 1.0 in the second period. The large aftershocks seen in the first period at a depth of 9 km on the Awaji side also result in smaller aftershock sequences of their own in the second period.

#### CALCULATION OF THE STATIC STRESS CHANGE

We calculate the changes in the Coulomb failure function,  $\Delta\text{CFF}$  from the dislocation model of the mainshock.  $\Delta\text{CFF}$  is expressed as

$$\Delta\text{CFF} = \Delta\tau - \mu' \Delta\sigma, \quad (7)$$

where  $\Delta\tau$  is the static shear stress change,  $\Delta\sigma$  is the static normal stress change, and  $\mu'$  is the apparent coefficient of friction. The derivation of this equation is fully described in the studies of King et al. (1994), Oppenheimer et al. (1988), and Simpson and Reasenber (1994). Positive values of  $\Delta\text{CFF}$  indicate movement toward failure, while negative values indicate movement away from failure. If  $\Delta\text{CFF}$  takes positive values in the regions where the faults of the aftershocks are distributed, the fault distribution is consistent with the mainshock-induced stress changes.

In the mainshock region, at least before the mainshock, the maximum principal axis of the regional stress orients east and west in the studied region (i.e., Hujita, 1968; Kishimoto, 1973; Nakane, 1973, Research Group for Active Faults of Japan, 1996). Figure 14c shows that the focal mechanism of the mainshock determined by Cho et al. (1995) clearly reflects the orientation of the maximum principal axis the regional stress. The strike directions of many active faults in the mainshock region (Research Group for Active Faults of Japan, 1996) agree well with the strike direction of the mainshock. Figure 14a and Figure 14b show the P and T axes of the focal mechanisms of the aftershocks in the mainshock region within 5 days after the mainshock

(Katao et al., 1996). We can see the tendency that the P axes of the focal mechanisms of the large aftershocks orient east and west horizontally, as well as that of the mainshock (Fig. 14c). When the smaller aftershocks are included, the focal mechanisms show great diversity, but yet we can see the tendency that the P axes orient east and west horizontally (Fig. 14a). Thus, the orientation of a nodal plane of focal mechanism in which the P axis orients east and west horizontally can be considered to approximate the orientation of preexisting weak zone in the studied region that is close to failure. We assume that the preexisting weak zone of specified orientation is uniformly distributed in the studied region. In the calculation of  $\Delta\text{CFF}$ , we examine right-lateral strike slip on a vertical fault striking N50°E and reverse slip on faults dipping 45° striking N0°E.

Under an assumption that the confining stress equals the normal stress, the apparent coefficient of friction  $\mu'$  is related to the coefficient of friction  $\mu$  by  $\mu' = \mu(1 - B)$ , where B is Skempton's coefficient (Simpson and Reasenber, 1994). B would be unity for water saturated solids but can be substantially less for rocks, constituents of which are not effectively incompressible (Rice and Clearly, 1976). Thus,  $\mu'$  takes lower value than laboratory values of  $\mu$  that range from about 0.6 to 0.85 (Byerlee, 1978). Reasenber and Simpson (1992) finds that low values from 0.1 to 0.3 are optimal for the 1989 Loma Prieta earthquake, California. King et al. (1994) suggests that the calculation results do not depend much on  $\mu'$  ranging from 0.0 to 0.75 for the 1992 Landers earthquake, California. Hashimoto (1997) uses  $\mu'$  of 0.4 for the 1995 Hyogo-ken Nanbu earthquake. In this study the results for  $\mu'$  from 0.0 to 0.8 are compared, and we find that the conclusions change only in detail; we illustrate the results for  $\mu' = 0.4$ .

Figure 15 shows the resulting distributions of  $\Delta\text{CFF}$ . At a depth of 14 km on the Kobe side, positive values of  $\Delta\text{CFF}$  for strike slip on a vertical fault are located along the fault distribution, showing consistency with mainshock-induced stress changes. However, the distributions of  $\Delta\text{CFF}$  are mostly inconsistent with the fault distribution at depths from 4 to 9 km. Instead, the distributions of  $\Delta\text{CFF}$  for reverse slip on faults dipping 45° can explain the fault distribution at a depth of 9 km, but a depth of 4 km. On the Awaji side, the distributions of  $\Delta\text{CFF}$  for reverse slip on faults dipping 45° explain the fault distribution fairly well, while that for strike slip on a vertical fault can not explain the fault distribution near the southwest edge of the mainshock

rupture. In conclusion, the fault distribution can be explained well in every region but at a depth of 4 km on the Kobe side, assuming strike slip on a vertical fault or reverse slip on faults dipping  $45^\circ$ . We can say that at least the large aftershocks are triggered by mainshock-induced stress change.

Following JMA (1995), the focal mechanism of a large aftershock (M 4.8) about 0.5 h after the mainshock, which occurred on the edge of the mainshock rupture beneath Awaji Island, is reverse slip quite similar to that assumed in the calculation of  $\Delta\text{CFF}$ . The focal mechanisms of aftershocks within 5 days after the mainshock (Katao et al., 1996) show a tendency that reverse slip is more prominent on the Awaji side than strike slip. Following Takahashi et al. (1996) the focal mechanisms beneath the Awaji Island and Akashi strait show the same tendency. This tendency of the focal mechanisms is consistent with the analyzed results in which the fault distribution is explained more satisfactorily by the distributions of  $\Delta\text{CFF}$  for reverse slip on faults dipping  $45^\circ$  on the Awaji side, rather than by the distributions of  $\Delta\text{CFF}$  for strike slip on a vertical fault.

## DISCUSSION

There are several studies on the dislocation model of the 1995 Hyogo-ken Nanbu earthquake (Horikawa et al., 1996; Ide et al., 1996; Sekiguchi et al., 1996; Wald, 1996; Yoshida et al., 1996). Horikawa (1998) examines the differences in rupture geometry that are assumed in these studies, and compares the resulting dislocation models in detail. In this study, the dislocation model of the 1995 Hyogo-ken Nanbu earthquake is examined using the three-dimensional rupture geometry estimated by CN98. The rupture geometry assumed is different from study to study, but the resulting dislocation models, including that obtained in this study, have resemblance. These results commonly deny the possibility of large slip in the shallow region on the Kobe side beneath the severely damaged zone, supporting that structural effects contribute the most to the generation of the severely damaged zone as suggested by several studies (e.g., Kawase et al., 1998; Pitarka et al., 1996).

In general bends or discontinuities are obviously impediment to rupture. Figure 16 shows that large slip in the shallow region beneath Awaji Island, in the deep region beneath Akashi

strait, and in the deep region on the Kobe side is distributed in the regions having less bends or discontinuities. As shown in Figures 10 and 16, there are bends on both sides of the initial rupture point. The bends on the Awaji and Kobe sides respectively correspond to an extensional jog and a compressional jog. Interrupted by both jogs, the rupture would propagate upward along more planar surface (Fig. 16). The direction of the rupture propagation might be related to the fact that a compressional jog is more serious impediment to rupture (Scholtz, 1990). We can not see significant slip in the region at a depth about 9 km along the pass between the initial rupture point and the shallow region of large slip beneath the Awaji Island, but it is interesting that the region corresponds to the region of high-frequency (0.1-0.5 s) radiation process according to Kakehi et al. (1996). The high-frequency radiation can not be identified in this study because the data period of the strong-motion waveforms used in this study is longer than 2 s.

The faults on which the aftershocks occur tend to cluster not only near the edges but also near the bends, precluding post-mainshock motion along the mainshock rupture of large slip. The faults of the aftershocks cluster in the regions that connect adjoining mainshock ruptures because such discontinuities in the mainshock rupture would result in increased local stress (e.g., Mendoza and Hartzell, 1988; Reasenber and Ellsworth, 1982; Richins et al. 1987). The fault distribution suggests that the aftershocks occur on numerous small faults rather than on a simple planar fault surface. Then, the bends of the mainshock rupture on a large scale would be constituted of numerous small faults on finer scale than the scale that we can deal with, for example, strike slip duplexes.

The focal mechanisms of the small aftershocks of the 1995 Hyogo-ken Nanbu earthquake show great diversity (Fig. 14a). In the case of the 1989 Loma Prieta earthquake, California, Beroza and Zoback (1994) suggests that the focal mechanism diversity comes from an uniaxial stress field uniformly distributed in the mainshock region, where the maximum principal axis is normal to the mainshock rupture plane. As well known, there are several evidences that the crust of the San Andreas fault zone, which includes the mainshock region of the 1989 Loma Prieta earthquake, has significantly low strength (Brune et al., 1969; Lachenbruch and McGarr, 1990; Mount and Suppe, 1987; Sigh and Jahns, 1984; Zoback et al., 1987). In such a case post-mainshock stress

field tends to uniform in a mainshock region and normal to the mainshock rupture plane, and the aftershocks would be triggered by the mainshock-induced strength change (Beroza and Zoback, 1994). Note that this concept is inconsistent with the concept that the aftershocks are triggered by mainshock-induced stress change. Horikawa (1998) suggests the possibility that the focal mechanism diversity found in the Hyogo-ken Nanbu earthquake sequence comes from the same reason as suggested by Beroza and Zoback (1994). However, it would not be the case in the mainshock region of the 1995 Hyogo-ken Nanbu earthquake, because it is unlikely that the mainshock region of the 1995 Hyogo-ken Nanbu earthquake is as weak as the San Andreas fault zone.

In order to examine directly the possibility that such a stress field is generated in the mainshock region of the 1995 Hyogo-ken Nanbu earthquake, we estimate the post-mainshock regional stress using the focal mechanisms of the aftershocks by a method of Gephart and Folyth (1984). In the method of Gephart and Folyth (1984) a grid search of stress models is performed to find the one which requires the smallest total rotation of all fault planes that is needed to match observed and predicted slip directions.

It should be noticed that the method, as well as the other methods, is contingent on the assumption that the post-mainshock stress field is uniform in the mainshock region. This assumption is reasonable if the same stress field as suggested by Beroza and Zoback (1994) is generated in the mainshock region, while the assumption is inconsistent with the concept that the aftershocks are triggered by mainshock-induced stress change. Figure 17a and Figure 17b show the orientation of the principal axes of the stress tensors and the measure of relative stress magnitudes (Gephart and Folyth, 1984), which are obtained from the slip directions calculated from the focal mechanisms in Figure 14a and Figure 14b, respectively. In the analysis, each slip direction is evenly weighted, and one of the nodal planes from each focal mechanism is automatically identified as a more reasonable fault plane than the other for a given stress model.

Figure 17a shows that the best orientation of the maximum principal axis has great resemblance to the orientation of P axis of the focal mechanism of the mainshock (Fig. 14c), but the orientation of the maximum principal axes above the 95 % confidence limit shows large diversity. The measure of relative stress magnitudes indicates that the stress field in the mainshock region

would be triaxial. These results would indicate the possibility that the small aftershocks are triggered by the mainshock-induced strength change in a triaxial stress field without resolved shear stress. Figure 17b shows that the respective orientation of maximum and minimum principal axes obtained from the focal mechanisms of the large aftershocks have great resemblance to the orientation of P and T axes of the focal mechanism of the mainshock. That is, the maximum principal axis is not normal to the mainshock rupture plane. The measure of relative stress magnitudes indicates that the stress field in the mainshock region would be triaxial rather than uniaxial. These results strongly suggest that the large aftershocks are triggered by the mainshock-induced stress changes, and we can reject the hypothesis that the diversity of the focal mechanisms shown in Figure 14a comes from the same reason as suggested by Beroza and Zoback (1994).

Aftershocks are seldom seen in the regions of large slip. The faults of the aftershocks, in particular, of the large aftershocks, cluster in the regions near the bends and edges of the mainshock rupture. The orientation of P axes of focal mechanisms of the large aftershocks has a resemblance to that of the mainshock. The distribution of the faults on which the aftershocks occur is mostly consistent with the mainshock-induced stress changes. Then, we can conclude that at least large aftershocks are caused by the mainshock-induced stress changes.

The large aftershock sequences, including the aftershock sequences of their own, begin right after the mainshock and end rapidly. It is natural that the large aftershocks complete their sequences in a short time because they relax significant stress concentrations induced by the mainshock at a time. The aftershocks of the large aftershocks near the bend on the Awaji side is much smaller than those on the Kobe side. This fact can be explained from the rupture geometry, where the bends on the Awaji and Kobe sides respectively correspond to an extensional jog and a compressional jog. Because normal stress in an extensional jog is less than that in a compressional jog, aftershocks near the bend on the Awaji side tend to become large rather than aftershocks near the bend on the Kobe side. Then, the aftershock sequences of their own tend to be small on the Awaji side than on the Kobe side.

The possibility measure keeps high values in the regions at depths from 4 to 9 km on the Kobe side as compared to the other regions. In the region at a depth of about 9 km near the bend

on the Kobe side, which corresponds to a compressional jog, the pore pressure is increased with the increase of elastic normal stress within a short time where fluid flow can be ignored. Stress corrosion that is suggested by Das and Scholtz (1981) becomes enhanced. As the special case, coseismic hydraulic fracturing would occur (Sibson, 1981), and then the strength is additionally lowered. Then, aftershocks become easier to be triggered but at the same time, increased normal stress in a compressional jog prevents occurrence of aftershocks. In the region near the bend at a depth of about 9 km on the Kobe side the small aftershocks continue to occur in such a balance.

As fluid becomes saturated, fluid flow is promoted from the region of high pore pressure into the regions of lower pore pressure. Then, pore pressure is increased in the regions around the compressional jog on the Kobe side, resulting in decrease of the effective stress. The reason why the distributions of  $\Delta CFF$  is inconsistent with the fault distribution at depth of 4 km on the Kobe side would be that equation (7) can not be applied to the calculation of  $\Delta CFF$  due to the fact that the role of pore fluid is not explicitly considered in equation (7). In compressional regimes, the fault-valve behavior can occur favorably (Sibson, 1983; 1992). Fluid pressure may become suprahydrostatic or may approach lithostatic load due to a permeability barrier, and when rupture transects the permeability barrier across which transition to a suprahydrostatic regime may occur, upward discharge from overpressured regions of the crust would be promoted. Then, the diversity of the focal mechanisms of the small aftershocks would be explained using extremely increased fluid pressure.

It is difficult to determine the cause of the small aftershocks because the occurrence of small aftershocks are easily influenced by local-scale inhomogeneities in rupture geometry or in orientation of preexisting weak zones. However, the occurrence of the aftershocks in the shallow regions on the Kobe side would not be directly related with the mainshock-induced stress change, and is likely to be triggered by a change in pore pressure or a change in strength resulted from hydraulic fracturing.

## CONCLUSION

The distribution of the fault of the aftershocks of the 1995 Hyogo-ken Nanbu earthquake

suggests that the aftershocks occurred on numerous small faults rather than on a simple planar fault surface. Not depending on the data period, the faults of the aftershocks are not distributed in the regions of large slip of the mainshock, and the faults of at least the large aftershocks are distributed near the bends or edges of the mainshock rupture. The distribution of  $\Delta CFF$  reveals that the distribution of faults of the large aftershocks is consistent with the mainshock-induced stress changes. There are several clusters of faults of aftershocks in the shallow regions at depths from 4 to 9 km on the northeast side, which consist of the faults of the small aftershocks. They are triggered by the changes in pore pressure or hydraulic fracturing induced by an interaction between the rupture geometry of the mainshock and pore fluid.

#### ACKNOWLEDGMENTS

I am grateful to Ichiro Nakanishi for illuminating discussions and Akira Yamada for comments leading to an improved manuscript. I give special thanks to Kazuo Oike for creating a pleasant research environment, and wish to thank Takaki Iwata, Yuko Kase and Takane Hori for their perceptive comments. I thank Hiroshi Katao for providing the valuable, unpublished aftershock data. This study was supported in part by Japan Society for the Promotion of Science.

#### REFERENCES

- Aki, K. (1979). Characterization of barriers on an earthquake fault, *J. Geophys. Res.*, **84**, 6140-6148.
- Beroza, G. C. and M. D. Zoback, (1993). Mechanism diversity of the Loma Prieta aftershocks of mainshock-aftershock interaction, *Science*, **259**, 210-213.
- Brune, J. N., T. L. Henyey, and R. F. Roy (1963). Heat flow, stress, and rate of slip along the San Andreas fault, California, *J. Geophys. Res.*, **74**, 3821-3827.
- Byerlee, J. (1978). Friction of rocks, *Pageoph.*, **116**, 615-626.
- Cho, I., I. Nakanishi, and K. Kanjo (1995). The source mechanism of the Hyogoken-nambu earthquake of January 17, 1995, *J. Nat. Disas. Sci.*, **16**, 21-29.
- Cho, I and I. Nakanishi (1998). Investigation of the three-dimensional fault geometry of the 1995 Hyogo-ken Nanbu earthquake using strong-motion and geodetic data, *in preparation*.

- Das, S. and C. H. Scholtz (1981). Theory of time dependant rupture in the earth, *J. Geophys. Res.*, **86**, 6039-6051.
- Davis, S. D. and C. Frohlich (1991). Single-link cluster analysis, synthetic earthquake catalogues, and aftershock identification, *Goephys. J. Int.*, **104**, 289-306.
- Feng, D., J. Gu, M. Ling, S. Xu, and X. Yu (1985). Assessment of earthquake hazard by simultaneous use of the statistical method and the method of fuzzy mathematics, *Pageoph*, **122**, 982-997.
- Feng, D. and M. Ichikawa (1989). Quantitative estimation of time-variable earthquake hazard by using fuzzy set theory, *Tectonophysics*, **169**, 175-226.
- Frohlich, C. and S. D. Davis (1990). Single-link cluster analysis as a method to evaluate spatial and temporal properties of earthquake catalogues, *Goephys. J. Int.*, **104**, 289-306.
- Gardner, J. K. and L. Knopoff (1974). Is the sequence of earthquakes in southern California, with aftershocks removed, Poissonian?, *Bull. Seismol. Soc. Am.*, **64**, 1363-1367.
- Gephart, J. W. and D. W. Folyth (1984). An improved method for determining the regional stress tensor using earthquake focal mechanism data: application to the San Fernando earthquake sequence, *J. Geophys. Res.*, **89**, 9305-9320.
- Hartzell, S. H. and T. H. Heaton (1983). Inversion of strong ground motion and teleseismic waveform data for the fault rupture history of the 1979 Imperial Valley, California, earthquake, *Bull. Seismol. Soc. Am.*, **73**, 1553-1583.
- Hashimoto, M. (1997). Correction to "Static stress changes associated with the Kobe earthquake: calculation of changes in Coulomb failure function and comparison with seismicity change", *Zisin (J. Seism. Soc. Japan), Ser. 2*, **50**, 21-27 (in Japanese with English abstract and figure captions).
- Hashimoto, M., T. Sagiya, H. Tsuji, Y. Hatanaka, and T. Tada (1996). Co-seismic displacements of the 1995 Hyogo-ken Nambu earthquake, *J. Phys. Earth*, **44**, 255-279.
- Horikawa, H. (1998). A review on the 1995 Hyogo-ken Nanbu earthquake and its sequence: seismological view, *Mem. Geol. Soc. Japan*, **51**, 9-19 (in Japanese with English abstract and figure captions).
- Horikawa, H., K. Hirahara, Y. Umeda, M. Hashimoto, and F. Kasano (1996). Simultaneous

- inversion of geodetic and strong-motion data for the source process of the Hyogo-ken Nanbu, Japan, Earthquake, *J. Phys. Earth*, **44**, 455-471.
- Hoshiaba, M., M. Seino, M. Okada, and H. Ito (1993). A list of spacetime inter-relationship in earthquake occurrence and its applications, *Papers in Meteorology and Geophysics*, **44**, 83-90 (in Japanese with English abstract and figure captions).
- Hujita, K. (1968). Rokko movements and its appearance: intersecting structural patterns of southwest Japan and quantary crustal movements, *The quantary Research*, **7**, 248-260 (in Japanese with English abstract and figure captions).
- Ide, S., M. Takeo, and Y. Yoshida (1996). Source Process of the 1995 Kobe Earthquake: Determination of spatiotemporal slip distribution by Bayesian modeling, *Bull. Seismol. Soc. Am.*, **86**, 547-566.
- JMA (Japan Meteorological Agency) (1995). The 1995 Hyogoken-Nanbu earthquake and its aftershocks, *Report of the Coordinating Committee for Earthquake Prediction*, **54**, 584-592.
- Takehi, Y., K. Irikura, M. Hoshiaba (1996). Estimation of high-frequency wave radiation areas on the fault plane of the 1995 Hyogo-ken Nanbu earthquake by the envelope inversion of acceleration seismograms, *J. Phys. Earth*, **44**, 505-517.
- Katao., H., N. Maeda, Y. Hiramatsu, Y. Iio and S. Nakao (1997). Detailed mapping of focal mechanisms in/around the 1995 Hyogo-ken Nanbu earthquake rupture zone, *J. Phys. Earth*, **45**, 105-119.
- Kawase, H., S. Matsushima, R. W. Graves, and P. G. Somerville (1998). Three-dimensional wave propagation analysis of simple two-dimensional basin structures with special reference to the 'the basin-edge effect', *Zisin (J. Seism. Soc. Japan)*, Ser. 2, **50**, 431-449 (in Japanese with English abstract and figure captions).
- King, G. C. P., R. S. Stein, and J. Lin (1994). Static stress changes and triggering of earthquakes, *Bull. Seismol. Soc. Am.*, **84**, 935-953.
- Kishimoto, Y. (1973). Seismicity and tectonic stress field in the Kansai District, southwest Japan, *Disas. Prev. Res. Inst. Annu.*, **16**, 9-21 (in Japanese with English abstract and figure captions).
- Lachenbruch, A. H. and A. McGarr (1990). Stress and heat flow, *U. S. Geol. Surv. Prof. Pap.*,

1515, 261-277.

- Lawson, C. L. and R. J. Hanson (1974). *Solving Least Squares Problems*, Prentice Hall, Inc., New Jersey.
- MacKenzie, D. P. (1969). The relation between fault plane solutions for earthquakes and directions of the principal stresses, *Bull. Seismol. Soc. Am.*, **59**, 591-601.
- Mendoza, C. and S. H. Hartzell (1988). Aftershock patterns and mainshock faulting, *Bull. Seismol. Soc. Am.*, **78**, 1438-1449.
- Molchan, G. M. and O. E. Dmitrieva (1992). Aftershock identification: methods and new approaches, *Geophys. J. Int.*, **109**, 501-516.
- Mount, V. S. and J. Suppe (1987). State of stress near the San Andreas fault: Implications for wrench tectonics, *Geology*, **15**, 1143-1146.
- Nakane, K. (1973). Horizontal tectonic strain in Japan (II), *J. Geodetic Soc. Japan*, **19**, 200-208 (in Japanese with English abstract and figure captions).
- Nemoto, Y., H. Katao, E. Suzuki, Y. Yoshida, and K. Irikura (1996). The spreading of aftershocks area directly after the 1995 Hyogo-ken Nanbu earthquake, *Programme and abstracts, the seismological society of Japan*, No 2, C67 (in Japanese).
- Olson, A. H. and R. W. Apsel (1982). Finite faults and inverse theory with applications to the 1979 Imperial Valley earthquake, *Bull. Seismol. Soc. Am.*, **72**, 1969-2001.
- Oppenheimer, D. H., P. A. Reasenber, and R. W. Simpson (1988). Fault plane solution for the 1984 Morgan Hill, California, earthquake sequence: evidence for the state of stress on the Calaveras fault, *J. Geophys. Res.*, **93**, 9007-9026.
- Pitarka, A., T. Iwata, and T. Kagawa (1996). Basin structure effects in the Kobe area inferred from the modeling of ground motions from two aftershocks of the January 17, 1995, Hyogo-ken Nanbu earthquake, *J. Phys. Earth*, **44**, 563-576.
- Prozorov, A. G. and Dziewonski, A. M. (1982). Method of studying variations in the clustering property of earthquake: application to global seismicity, *J. Geophys. Res.*, **87**, 2829-2839.
- Reasenber, P (1985). Second-order moment of California Seismicity, 1969-1982, *J. Geophys. Res.*, **90**, 5479-5495.
- Reasenber, P. A. and W. L. Ellsworth (1982). Aftershocks of the Coyote Lake, California,

- earthquake of August 6, 1979: a detailed study, *J. Geophys. Res.*, **87**, 10637-10655.
- Reasenber, P. A. and R. W. Simpson (1992). Response of regional seismicity to the static stress change produced by the Loma Prieta earthquake, *Science*, **255**, 1687-1690.
- Research Group for Active Faults of Japan (1996). *Maps of active faults in Japan with an explanatory text*, University of Tokyo Press, Tokyo.
- Rice, J. R. and M. P. Clarly (1976). Some basic stress diffusion solutions for fluid-saturated elastic porous media with compressible constituents, *Reviews of geophysics and space physics*, **14**, 227-241.
- Richins, W. D., J. C. Pechmann, R. B. Smith, C. J. Langer, S. K. Goter, J. E. Zollweg, and J. J. King (1987). The 1983 Borah Peak, Idaho, earthquake and its aftershocks, *Bull. Seismol. Soc. Am.*, **77**, 694-723.
- Rybicki, K. (1973). Analysis of aftershocks on the basis of dislocation theory, *Phys. Earth. Plant. Interiors*, **7**, 409-422.
- Scholtz, C. H. (1990). *The mechanics of earthquakes and faulting*, Cambridge University Press, New York.
- Sekiguchi, H., K. Irikura, T. Iwata, Y. Kakehi, and M. Hoshiba (1996). Minute locating of faulting beneath Kobe and the waveform inversion of the source process during the 1995 Hyogo-ken Nanbu, Japan, earthquake using strong ground motion records, *J. Phys. Earth*, **44**, 473-487.
- Sibson, R. H. (1981). Fluid flow accompanying faulting: field evidence and models, in *Earthquake prediction an international review, M. Ewing Ser. 4*, edited by D. W. Simpson and P. G. Richards, pp. 593-603, American Geophysical Union, Washington D C.
- Sibson, R. H. (1985). Stopping of earthquake ruptures at dilatational fault jogs, *Nature*, **80**, 1580-1604.
- Sibson, R. H. (1990). Rupture nucleation on unfavorably oriented faults, *Bull. Seismol. Soc. Am.*, **80**, 1580-1604.
- Sibson, R. H. (1992). Implication of fault valve behaviour for rupture nucleation and recurrence, *Tectonophysics*, **211**, 283-293.
- Sieh, K. E. and R. H. Jahns (1984). Holocene activity of the San Andreas fault at Wallace

- Creek, California, *Geol. Soc. Amer. Bull.*, **95**, 883-896.
- Simpson, R. and P. Reasenberg (1994). Earthquake-induced static stress changes on central California faults, in *The Loma Prieta, California, earthquake of October 17, 1989 – tectonic process and models*, Simpson, R. W. (Editor), *U. S. Geol. Surv. Prof. Pap.*, **1515**, 261-277.
- Stevens, S. S. (1946). On the theory of scales measurement, *Science*, **103**, 677-680.
- Takahashi, N., K. Suyehiro, M. Shinohara, A. Kubo, A. Nishizawa and H. Matsuoka (1996). Aftershocks and faults of the Hyogo-ken Nanbu earthquake beneath Akashi strait, *J. Phys. Earth*, **44**, 337-347.
- Utsu, T. (1961). A statistical study on the occurrence of aftershocks, *Geophys. Mag.*, **30**, 521-605.
- Wald, D. J. (1996). Slip history of the 1995 Kobe, Japan, earthquake determined from strong motion, teleseismic, and geodetic data, *J. Phys. Earth*, **44**, 489-503.
- Yokota, S. and S. Masumoto (1984). Fuzzyness of geological data and its description, *Chikyu monthly*, **6**, 309-314 (in Japanese).
- Yokota, T. and H. Ito (1994). Application of fuzzy theory to the seismology, in *Fuzzy science*, Asai, K. (editor), Kaibundo, Tokyo, 191-213 (in Japanese).
- Yoshida, S., K. Koketsu, B. Shibazaki, T. Sagiya, and T. Kato (1996). Joint inversion of near- and far-field waveforms and geodetic data for the rupture process of the 1995 Kobe earthquake, *J. Phys. Earth*, **44**, 437-454.
- Zadeh, L. A. (1965). Fuzzy sets, *Information and Control*, **8**, 338-353.
- Zadeh, L. A. (1973). Outline of a new approach to the analysis of complex systems and decision processes, *IEEE Trans. Systems, Man, and Cybernetics*, **SMC-3**, 28-44.
- Zadeh, L. A. (1978). Fuzzy sets as a basis for a theory of possibility, *Fuzzy sets and Systems*, **1**, 3-28.
- Zoback, M. D., M. L. Zoback, V. S. Mount, J. Suppe, J. P. Eaton, J. H. Healy, D. H. Oppenheimer, P. Reasenberg, L. Jones, C. B. Raleigh, I. G. Wong, O. Scotti, and C. Wentworth (1987). New evidence on the state of stress of the San Andreas fault system, *Science*, **238**, 1105-1111.

## Figure Captions

- FIG. 1 Map of the strong-motion stations and the observation points of the geodetic data. Solid squares, triangles, and circles show the strong-motion stations deployed by DPRI, CE-ORKA and JMA, respectively. Open squares and circles correspond to GPS observation sites and triangulation points, respectively. Lines A, B, C, and D are the leveling routes. A star shows the hypocenter.
- FIG. 2 Rupture geometry, which is assumed based on three-dimensional estimation in CN98. (a) Rupture geometry viewed from above. Aftershocks that occurred within the rectangle are analyzed in this study. (b) Rupture geometry viewed from the direction of N140°E. The hypocenter is shown by a solid star. (c) Rupture geometry viewed from bird's eye.
- FIG. 3 Misfits between the observed and synthetic records of the geodetic and strong-motion data as a function of rupture velocity.
- FIG. 4 Dislocation models obtained from the inversion with  $W_g$  of 0, 1, 5, and infinity. Arrows show the movement of the southeast side against the northwest side.
- FIG. 5 Misfits between the observed and synthetic records of the geodetic and strong-motion data as a function of  $W_g$ .
- FIG. 6 Comparison between the observed (heavy line) and synthetic (thin line) displacement waveforms. The station code and the component are given on the trace. The start time of the trace from the origin time [s] and the peak amplitude of the observed waveform [cm] are given to the left and right of each trace, respectively.
- FIG. 7 Comparison between the observed (heavy line) and synthetic (thin line) static displacements: (a) The vertical static displacements, (b) the static line-length changes, and (c) the horizontal static displacements. The peak amplitudes of the observed static displacement [cm] are given on the left. The parts A, B, C, and D in (a) correspond to the routes A, B, C, and D in Figure 1, respectively. The parts A and B in (b) correspond to the stations

on the north side of Awaji Island and around Akashi strait. The points A, B, and C in (c) correspond to the records at MINOO, YOSHINO, and MITSU (Fig. 1), respectively.

FIG. 8 Membership functions. (a) and (b) show membership functions  $R^d$  for  $A^d = 0.091, 0.91,$  and  $9.1,$  and  $R^t$  for  $A^t = 0.045, 0.45, 4.5,$  and  $45,$  respectively. (c) and (d) show respective distributions of  $R$  defined by  $R^d \wedge R^t$  and  $R^d R^t,$  where  $A^d$  of  $0.91$  and  $A^t$  of  $0.45$  are used. Contours of grade of membership function  $R$  are drawn at intervals of  $0.025.$

FIG. 9 Vertical section of the fault distribution compared to the slip distribution of the mainshock (top), and the corresponding aftershock distribution (bottom). Contours of possibility measure are drawn at intervals of  $0.05.$  A star shows the hypocenter.

FIG. 10 (a) Horizontal sections of the rupture geometry of the mainshock and the fault distribution. Contours of possibility measure are drawn at intervals of  $0.05.$  A star shows the hypocenter. (b) Number of aftershocks used in the analysis.

FIG. 11 Horizontal sections of the rupture geometry of the mainshock and the fault distribution estimated taking the second maximum instead of maximum in equation (6). Contours of possibility measure are drawn at intervals of  $0.025.$

FIG. 12 Horizontal sections of the rupture geometry and the fault distribution estimated using data sets from which the small aftershocks are excluded, changing the lower limit of the magnitude ( $M_{low}$ ) from  $1.0$  to  $3.0.$  Contours of possibility measure are drawn at intervals of  $0.025.$

FIG. 13 Temporal variation in fault distribution. Contours of possibility measure are drawn at intervals of  $0.025.$

FIG. 14 Orientations of P (open circle) and T (solid circle) axes of the fault plane solutions (Equal area projection on lower hemisphere) of (a) all aftershocks within 5 days after the mainshock (Katao et al., 1996), (b) the aftershocks with the lower limit of the magnitude of  $3.5,$  and (c) the mainshock.

FIG. 15 Horizontal sections of the distribution of  $\Delta\text{CFF}$  within a rectangle in Figure 2a. Regions in black and red correspond to negative and positive  $\Delta\text{CFF}$ , respectively. The rupture geometry of a mainshock and the fault distribution in Figure 10a are also illustrated with white lines.

FIG. 16 Illustration of the relation between the rupture geometry and the slip distribution, which is taken from the dislocation model with  $W_g$  of 1.0 at rupture velocity of 3.4 km/s. Solid circles show bends or discontinuities. A cross shows the hypocenter.

FIG. 17 Orientation of the principal axes of stress tensors (Equal area projection on lower hemisphere), and the measure of relative stress magnitudes. The orientations of maximum ( $\sigma_1$ ), intermediate ( $\sigma_2$ ), and minimum ( $\sigma_3$ ) compression axes above the 95 % confidence limit are presented by solid circle, open circle, and cross. The best orientations are presented by square. The measure of relative stress magnitudes  $R$  is defined as  $R = (\sigma_2 - \sigma_1)/(\sigma_3 - \sigma_1)$ . (a) and (b) are obtained using the data sets of focal mechanisms in Figure 14a and Figure 14b, respectively.

Up  
↑

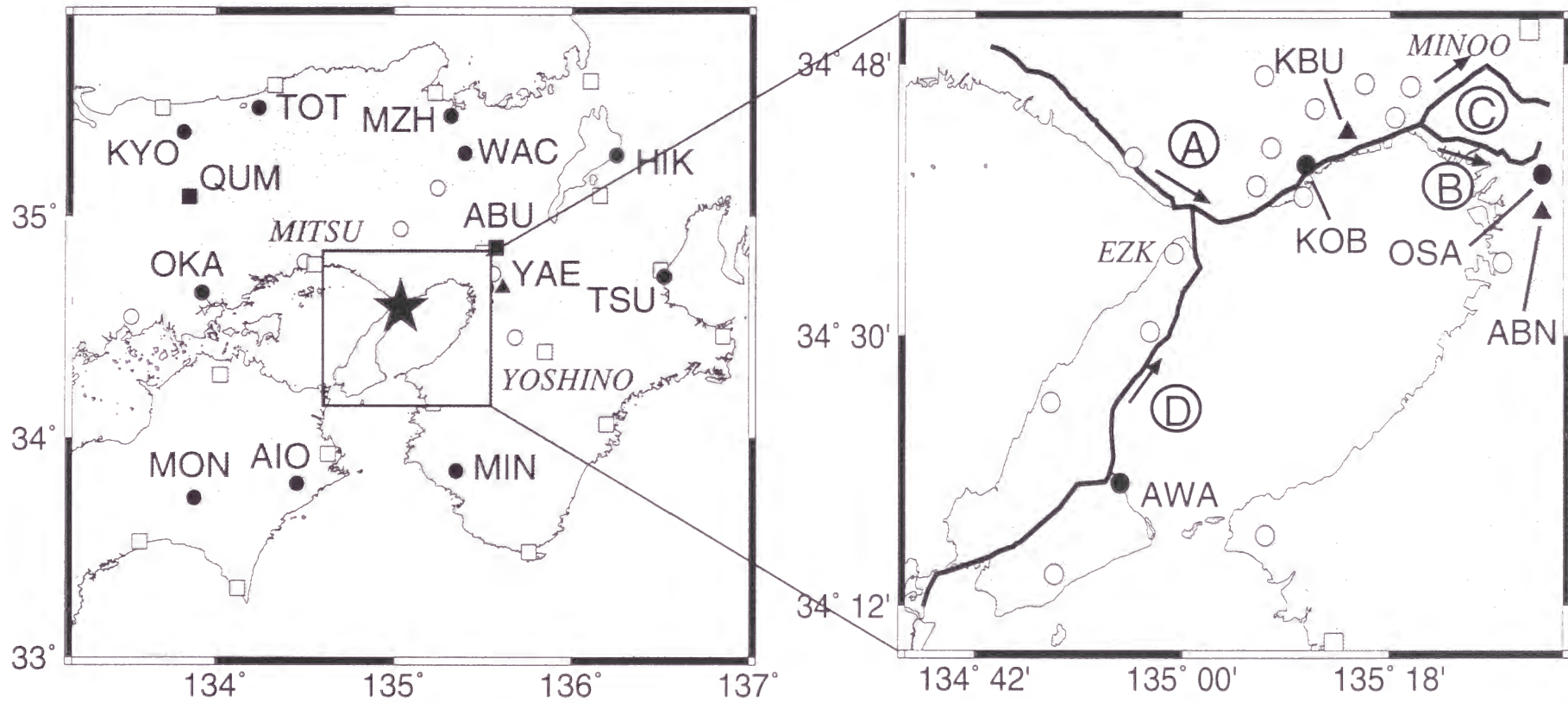
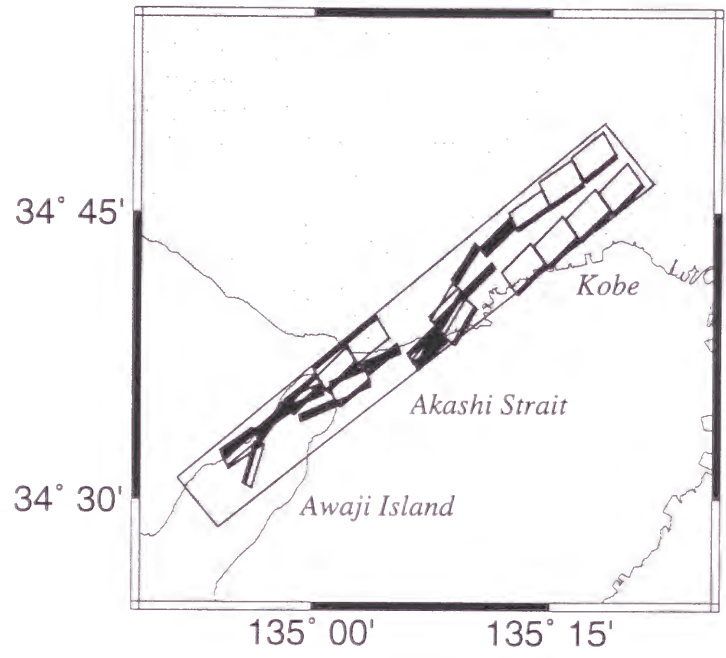
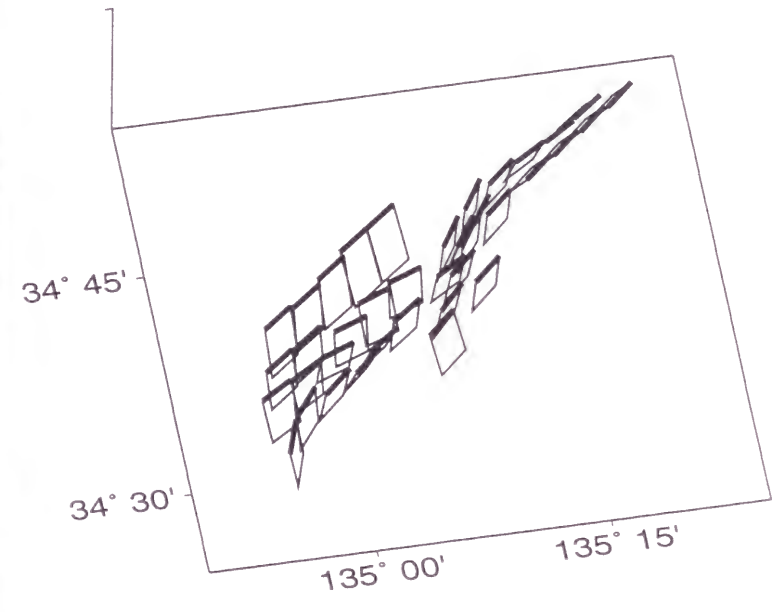


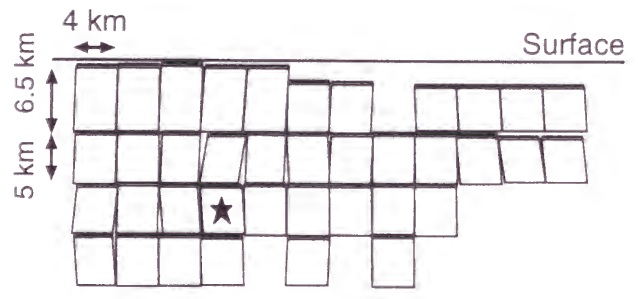
Fig. 1



(a)



(c)



(b)

Fig. 2

↑  
↑  
↑

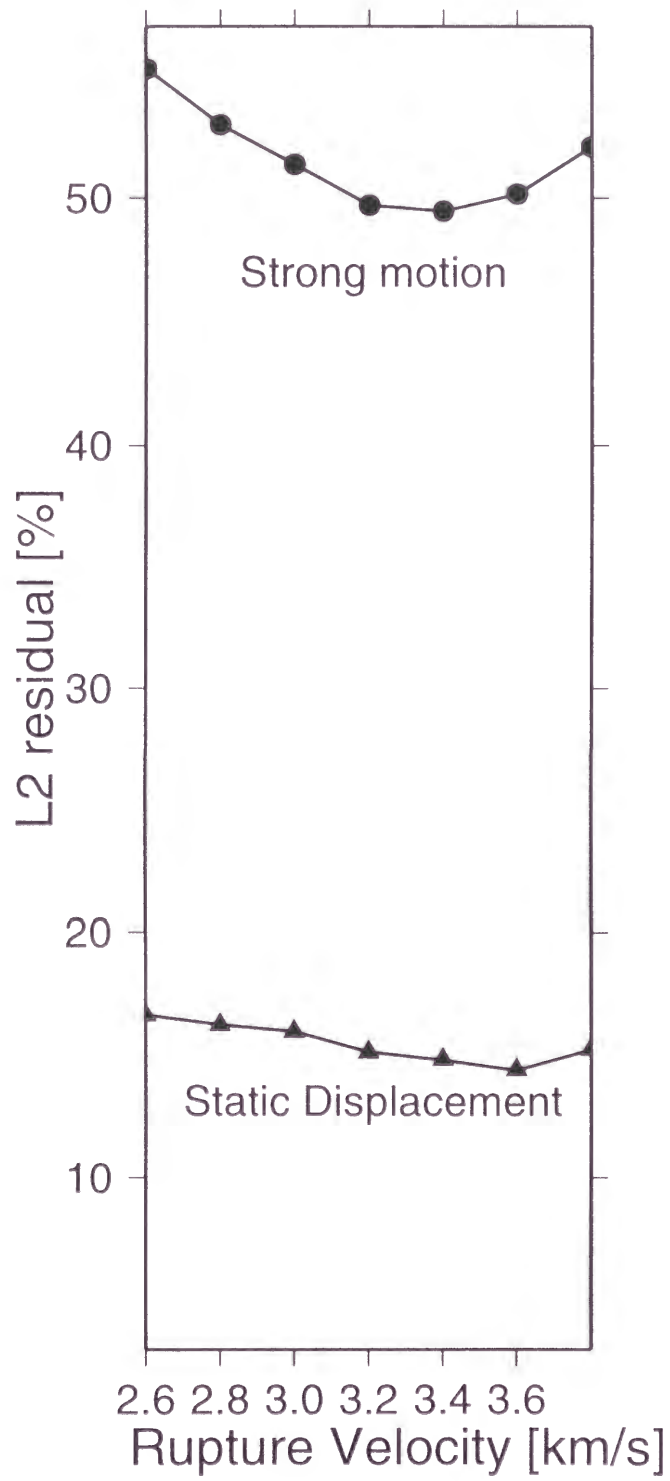


Fig. 3

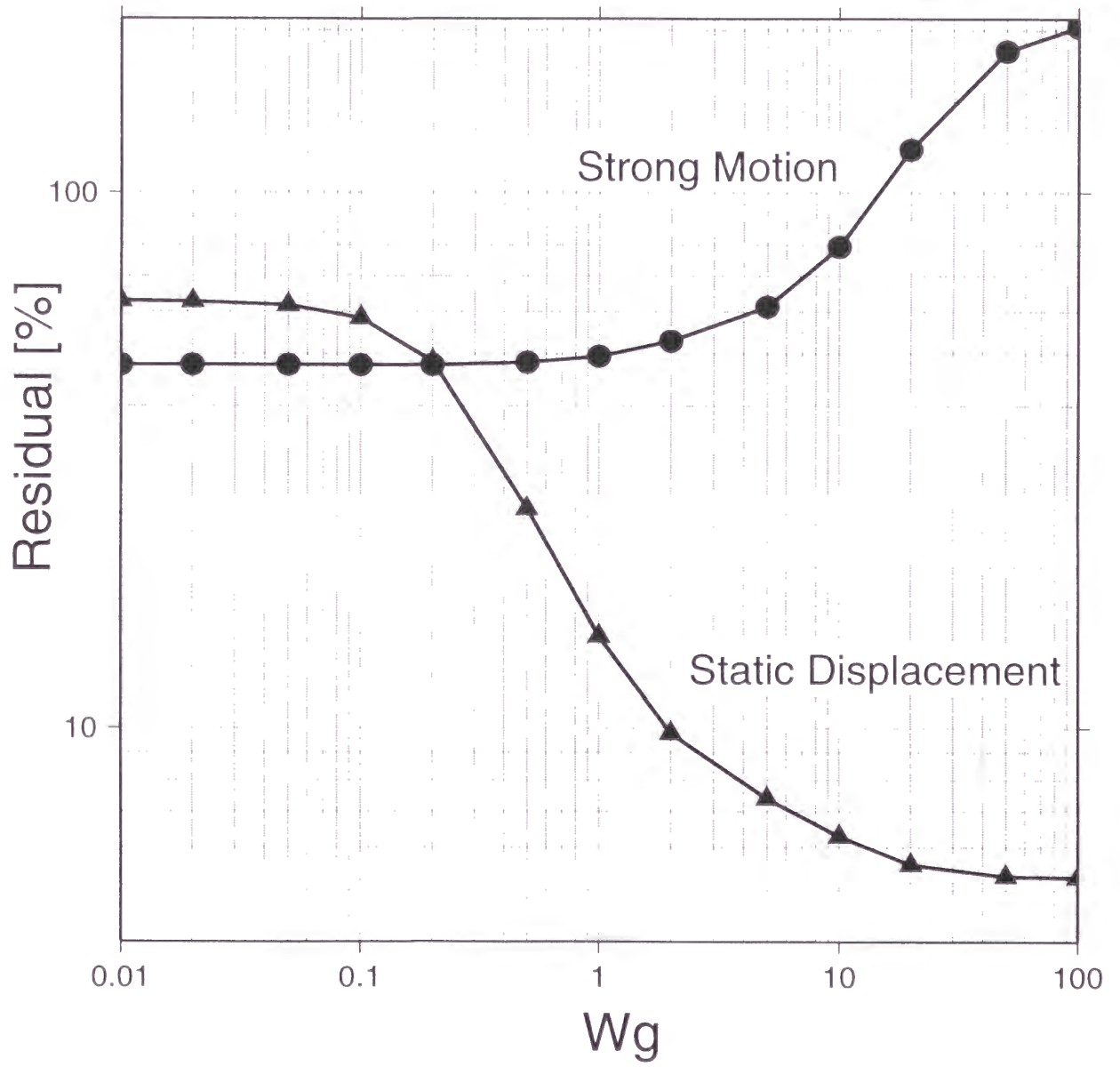
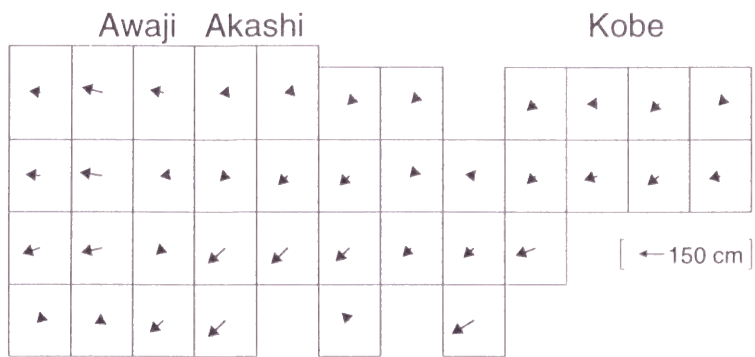
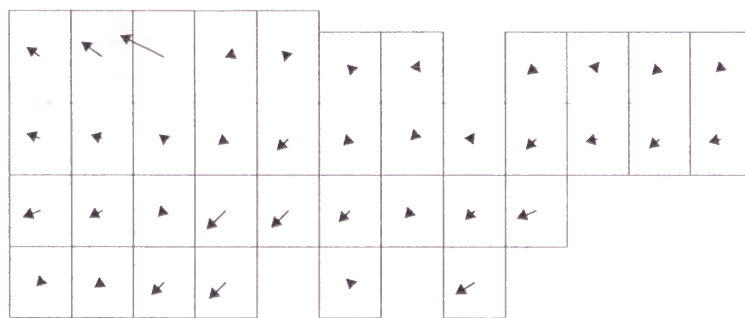


Fig. 4

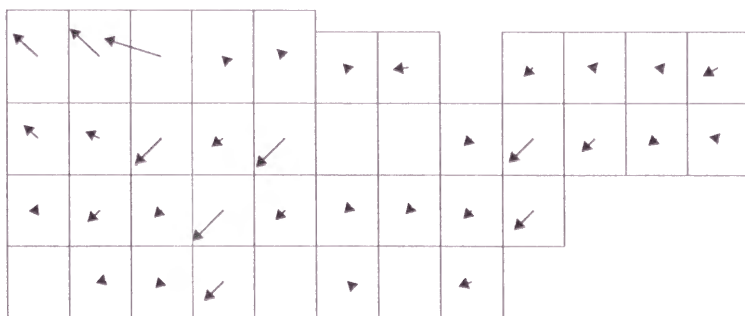
Fig. 4



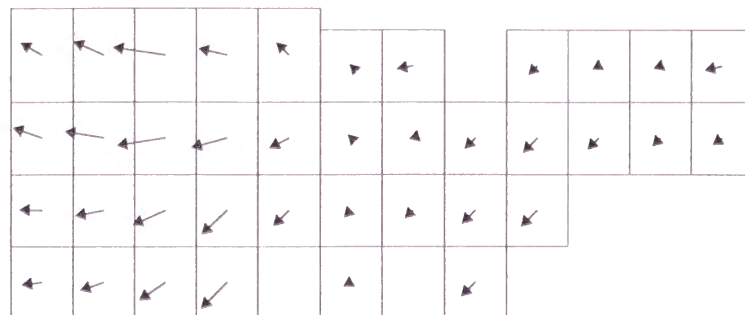
Strong Motion 1      Static Displacement 0



Strong Motion 1      Static Displacement 1



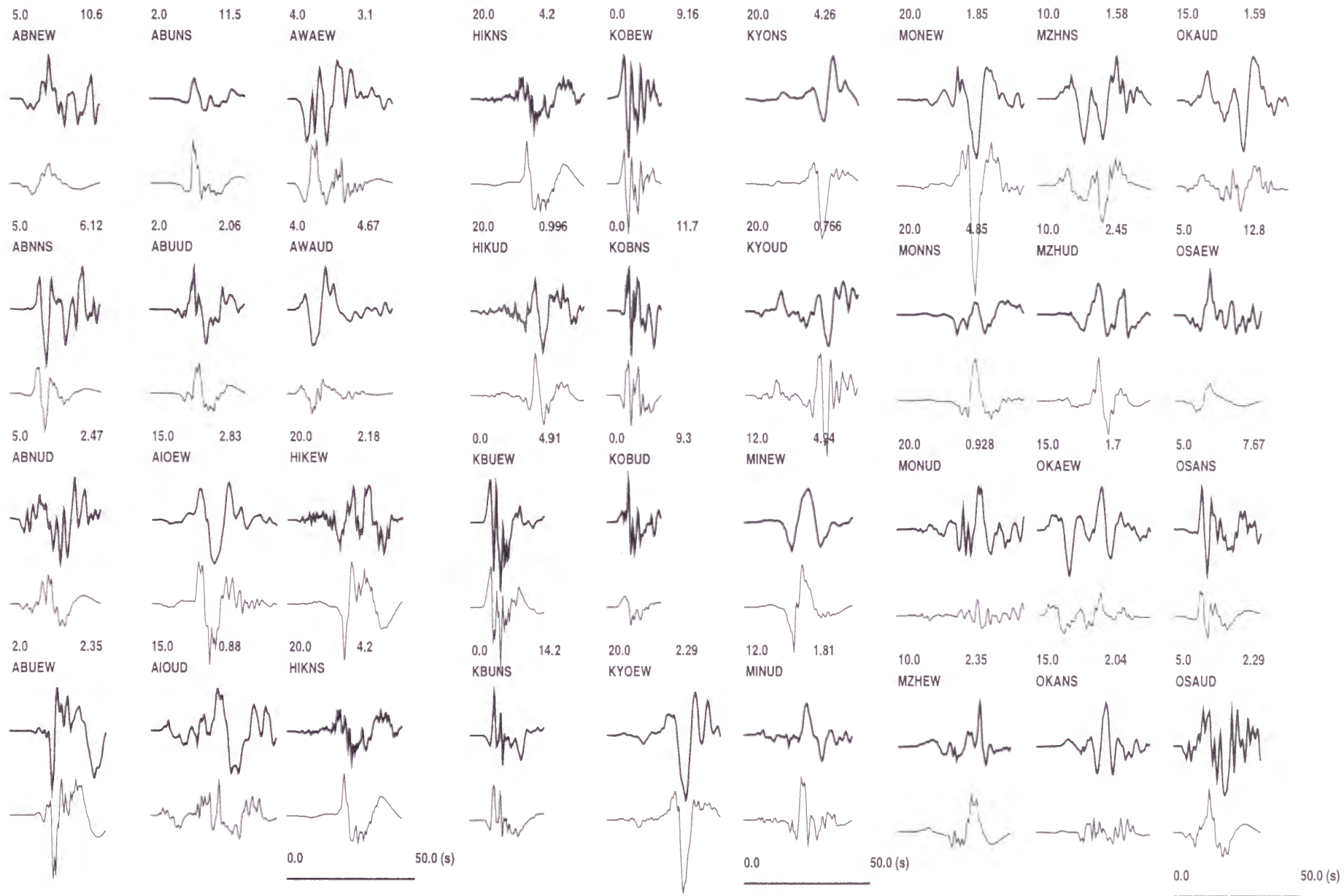
Strong Motion 1      Static Displacement 5



Strong Motion 0      Static Displacement 1

Fig. 5

Fig. 6



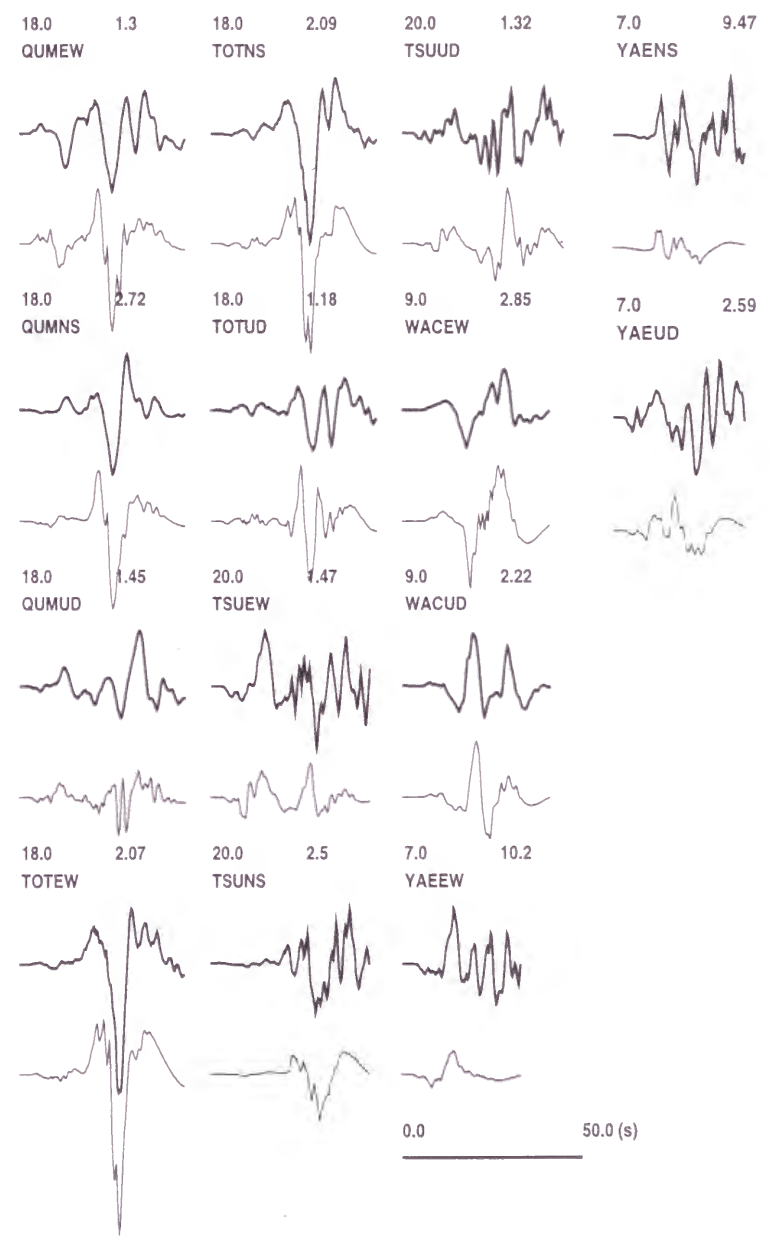


Fig. 6 (continued)

up ↑

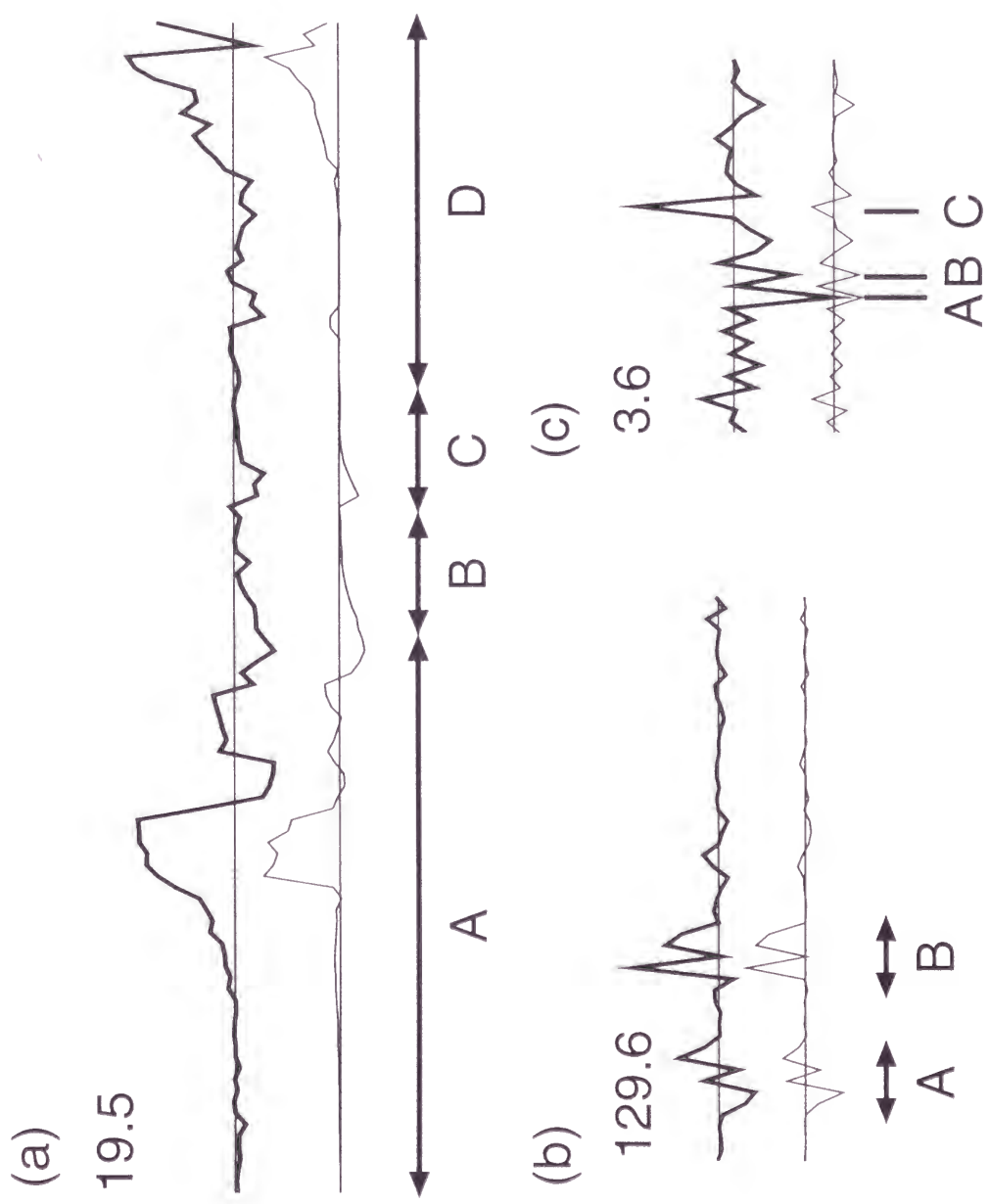
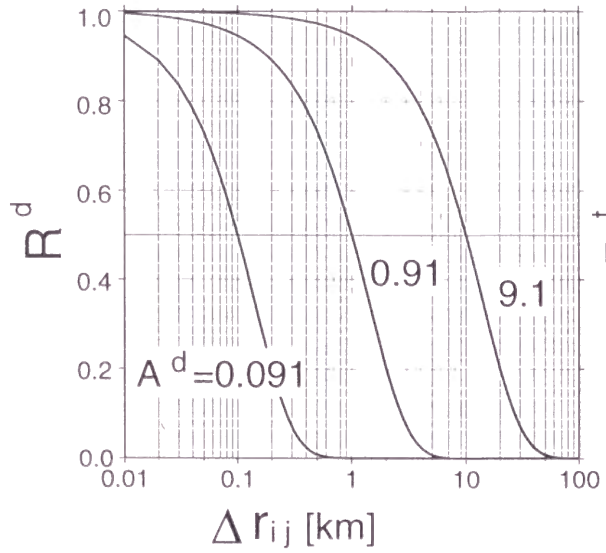
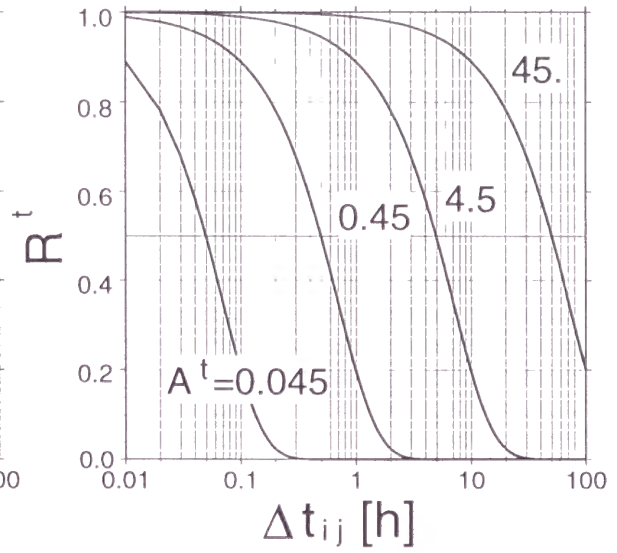


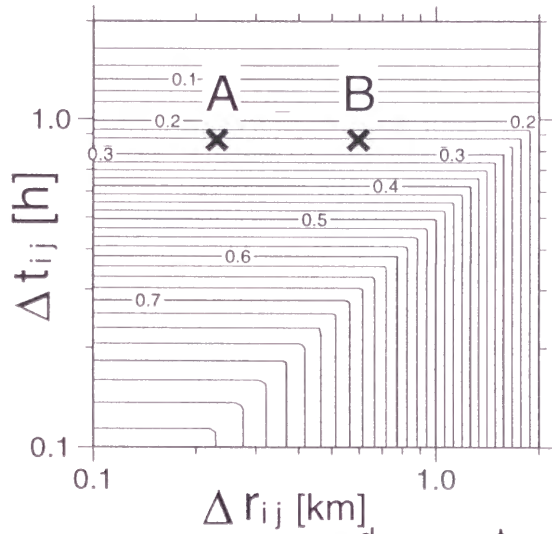
Fig. 7



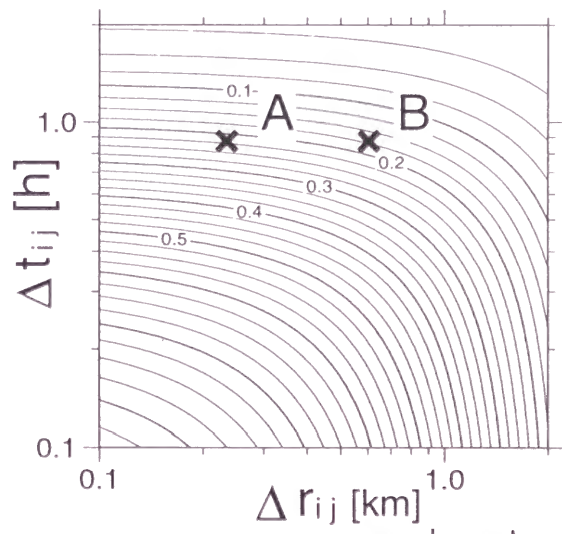
(a)



(b)



(c)  $R = R^d \wedge R^t$



(d)  $R = R^d R^t$

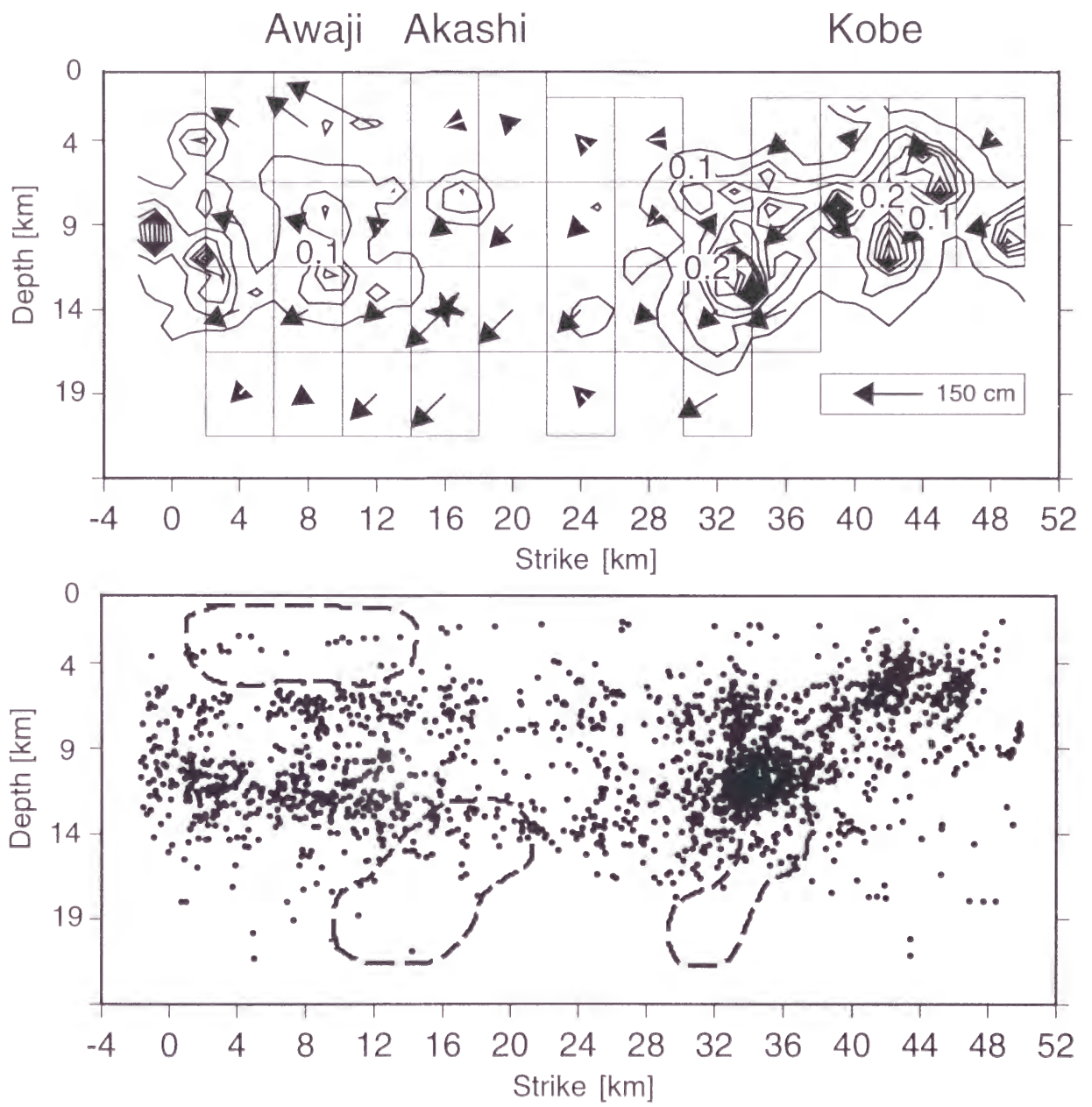


Fig. 9

Fig. 9

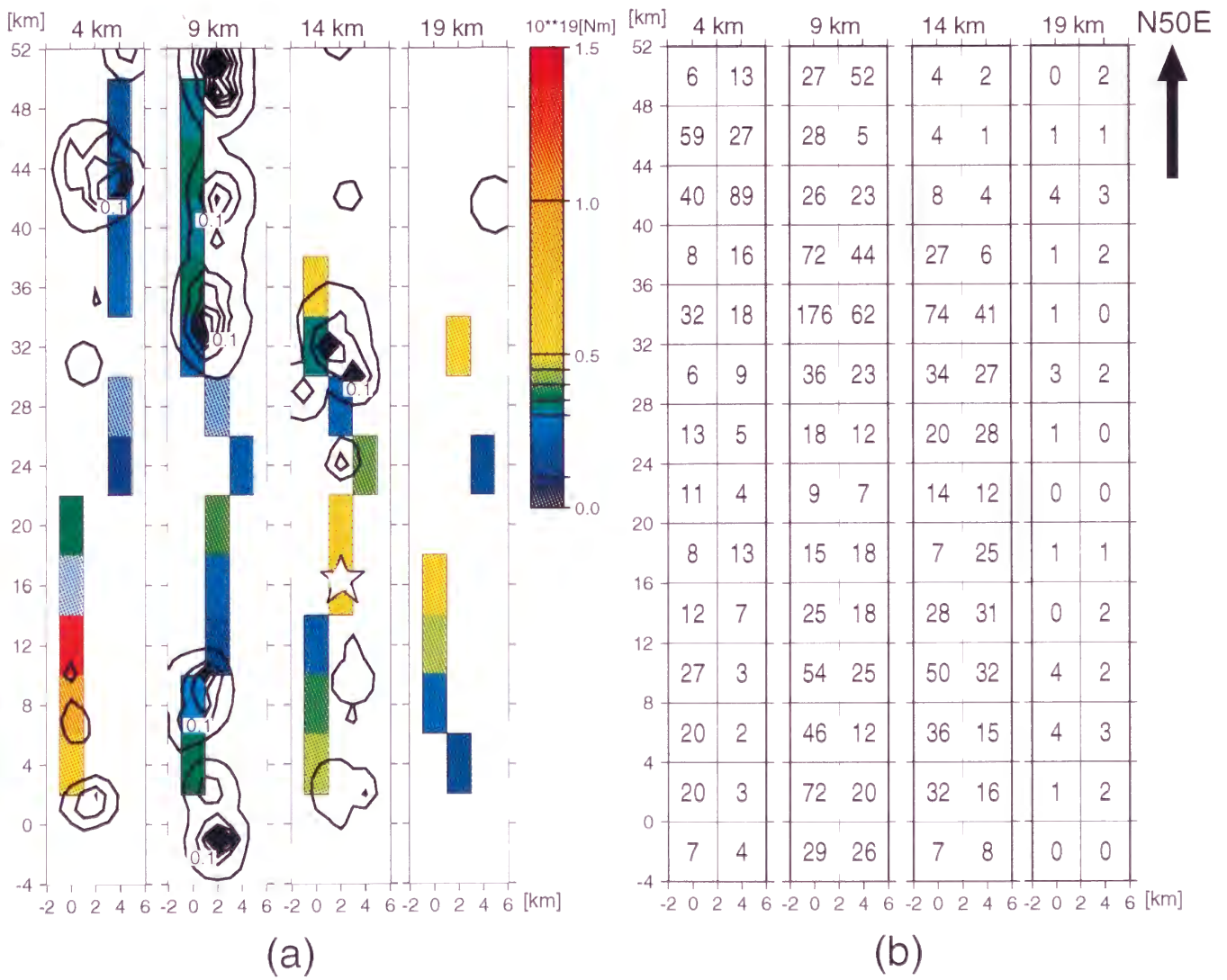


Fig. 10

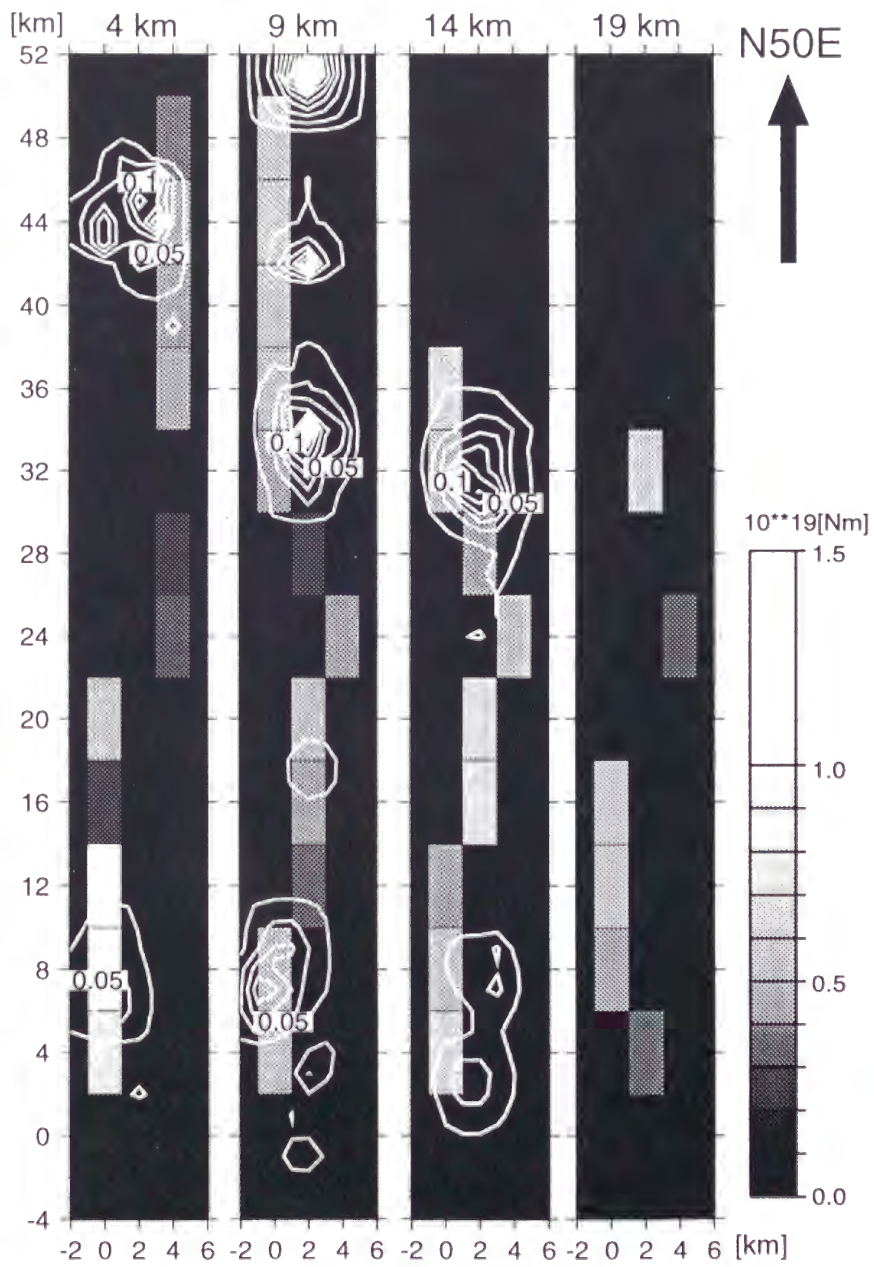


Fig. 11

Fig. 11

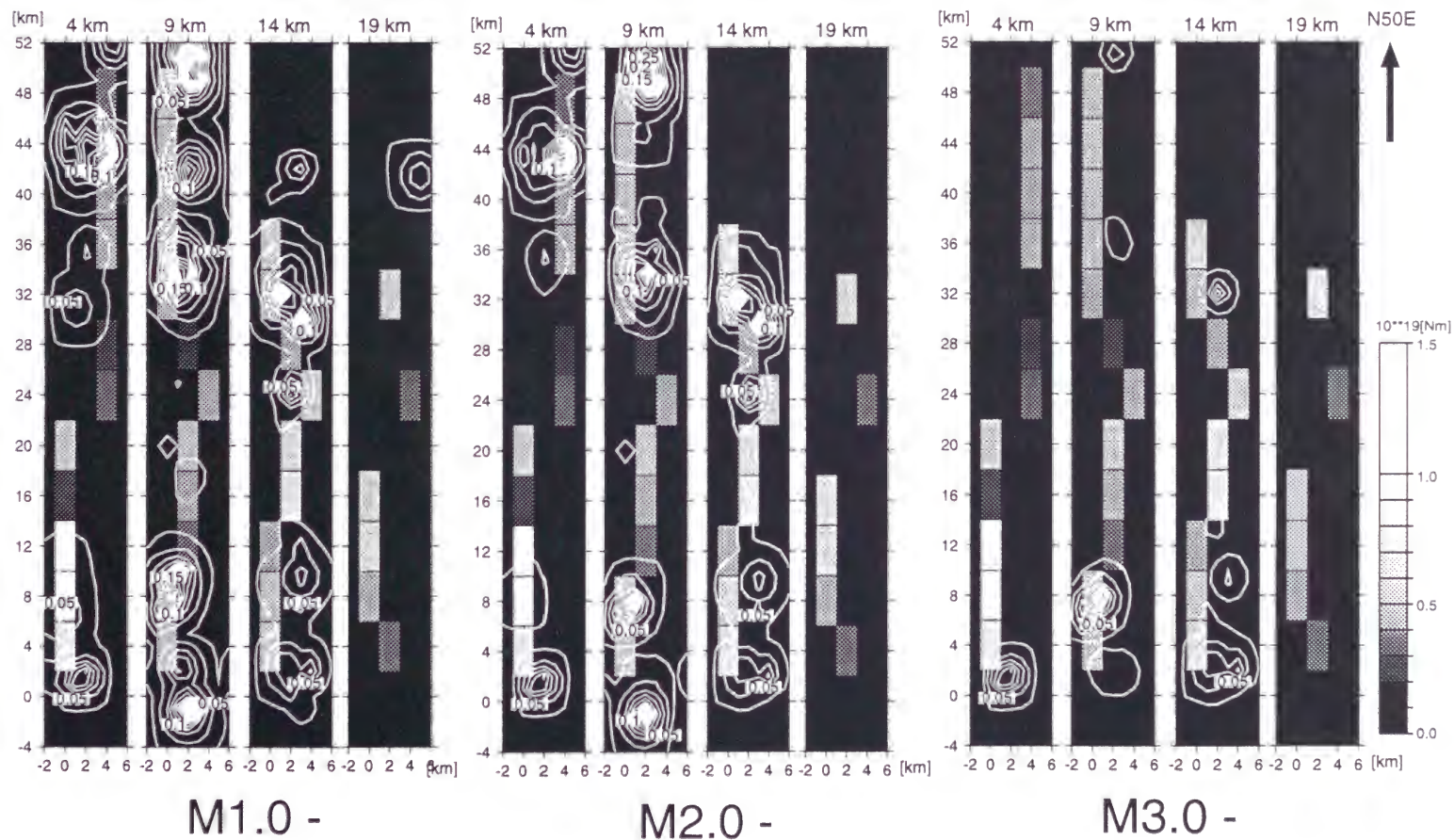


Fig. 12

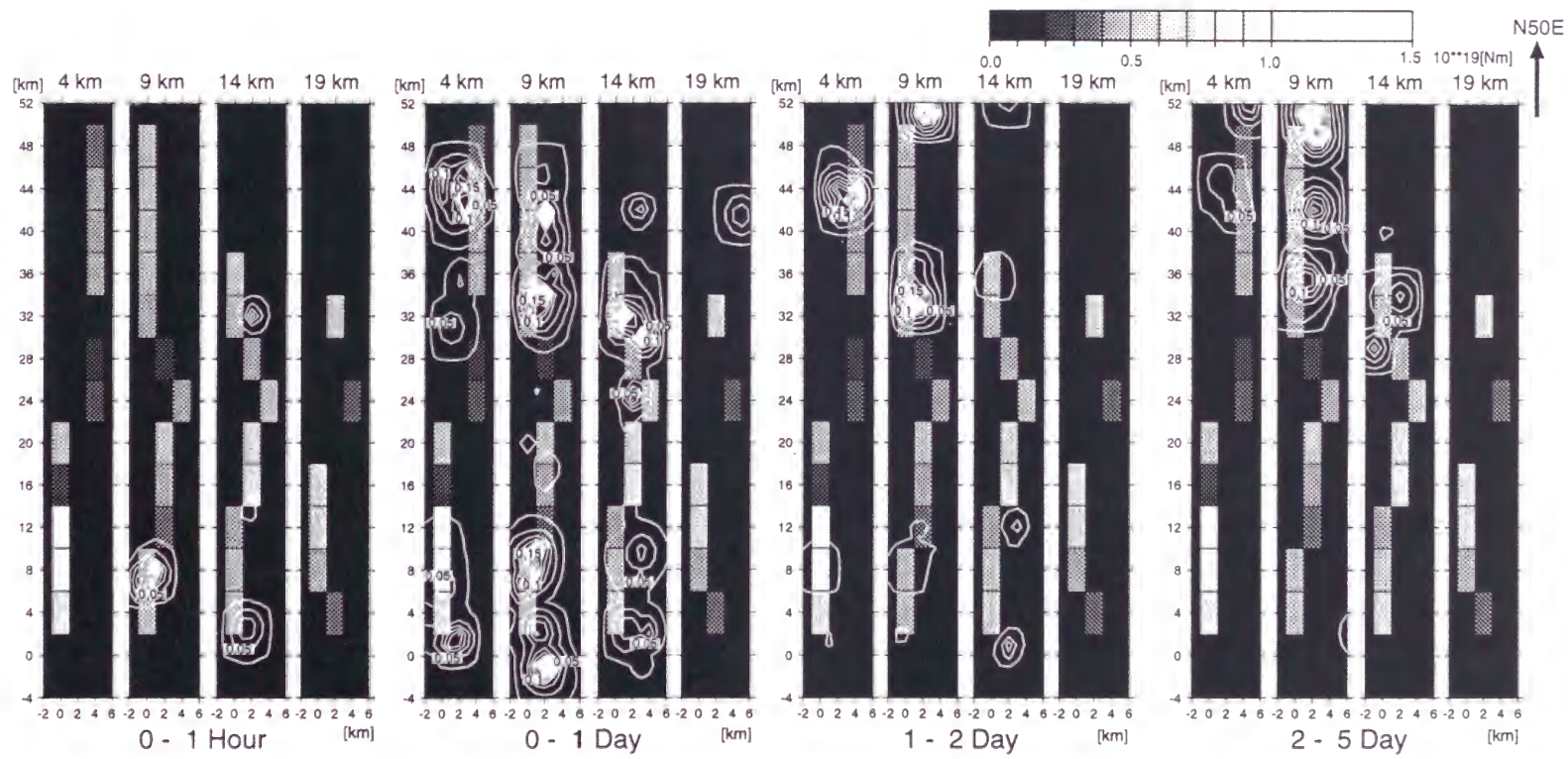
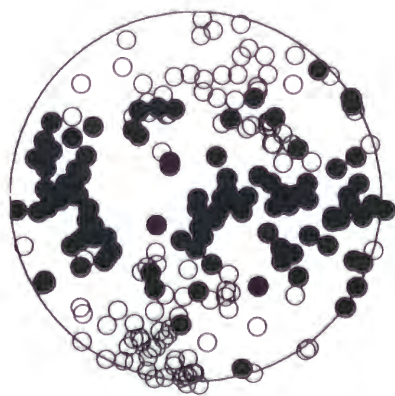
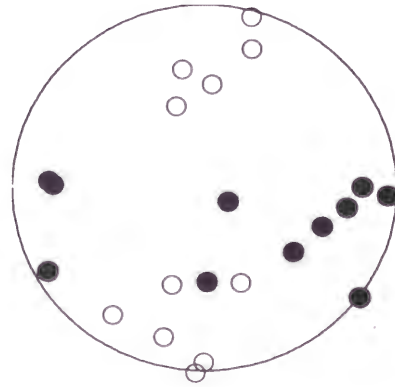


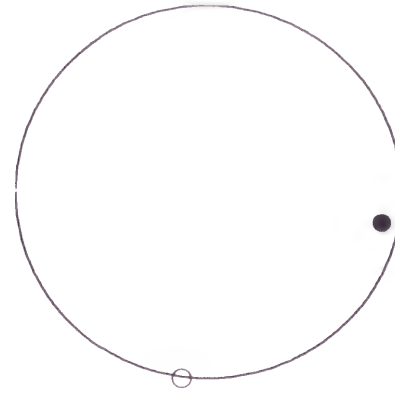
Fig. 13



(a) All (M2.0 -)

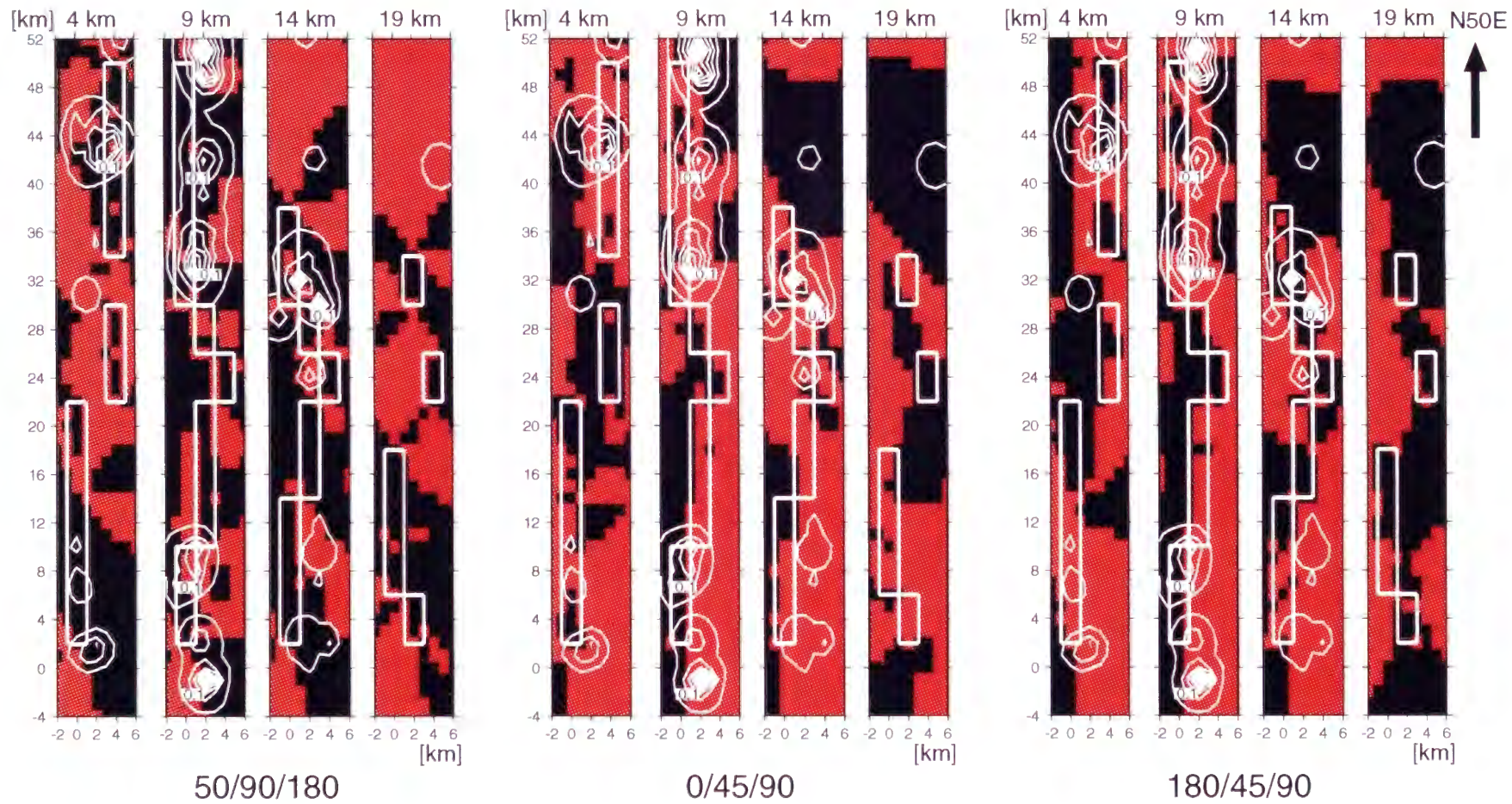


(b) M3.5 -



(c) Mainshock

Fig. 15





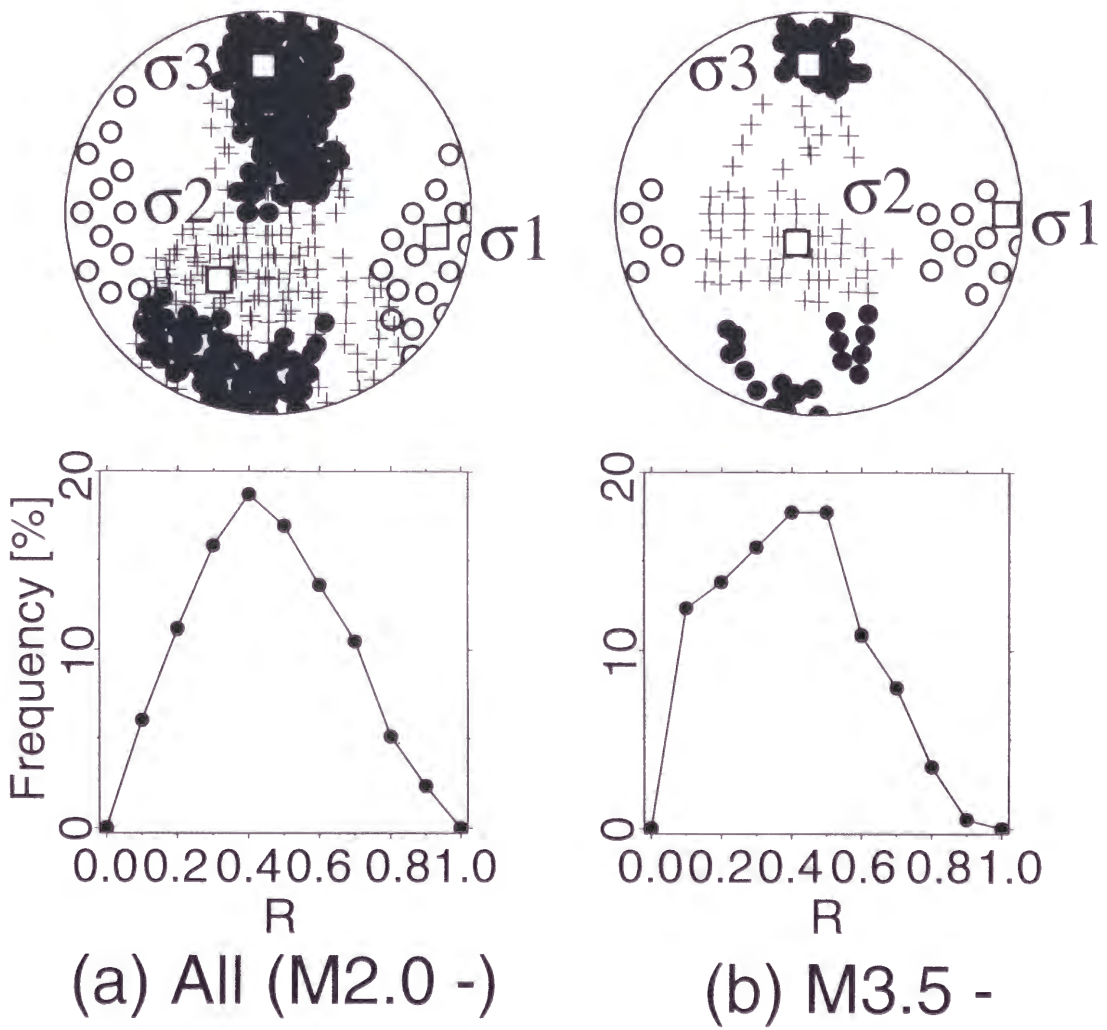


Fig. 17